THE HENRYK NIEWODNICZAŃSKI
INSTITUTE OF NUCLEAR PHYSICS
POLISH ACADEMY OF SCIENCES
UL. RADZIKOWSKIEGO 152, 31-342 KRAKÓW, POLAND

**WWW.IFJ.EDU.PL/BADANIA/PUBLIKACJE/RAPORTY/**

KRAKÓW, JULY 2020

---

REPORT NO 2105/AP

# Study of the mutual dependence between Lower Hybrid current drive and heavy impurity transport in tokamak plasmas. Part 1. Preparatory work and theoretical background

***A. JARDIN[1], J. BIELECKI[1], K. KROL[1], Y. PEYSSON[2], D. MAZON[2], D. DWORAK[1] & M. SCHOLZ[1]***

[1] INSTITUTE OF NUCLEAR PHYSICS POLISH ACADEMY OF SCIENCES (IFJ PAN), PL-31-342, KRAKOW, POLAND
[2] CEA, IRFM, F-13108, SAINT-PAUL-LEZ-DURANCE, FRANCE

**Abstract**

This document reports the activities performed during the year 2019-2020 in the framework of the HARMONIA 10 project entitled “Study of the mutual dependence between Lower Hybrid current drive and heavy impurity transport in tokamak plasmas” as well as the preliminary results obtained during the first year of project execution. The project is founded by the Polish National Science Centre (NCN) and carried out in a close collaboration with the foreign partner - Institute for Magnetic Fusion Research (IRFM) of the French Alternative Energies and Atomic Energy Commission (CEA).

**Wydano nakładem Instytutu Fizyki Jądrowej im. Henryka Niewodniczańskiego**
**Polskiej Akademii Nauk**
**Kraków 2020**

# Table of Contents:

# 1. Introduction - Aim and scope of the project

This document reports the activities performed during the year 2019-2020 in the framework of the HARMONIA 10 project entitled “Study of the mutual dependence between Lower Hybrid current drive and heavy impurity transport in tokamak plasmas” as well as the preliminary results obtained during the first year of project execution. The project is founded by the Polish National Science Centre (NCN) and carried out in a close collaboration with the foreign partner - Institute for Magnetic Fusion Research (IRFM) of the French Alternative Energies and Atomic Energy Commission (CEA). The results presented here are in a significant part inspired from the fruitful exchange and the synthesis in [Peysson 2019].

The tokamak device is currently the most advanced solution to control the fusion reaction and to harvest energy in the future. Among several possibilities, the following reaction:

$$ {}^{2}_{1}\mathrm{D} + {}^{3}_{1}\mathrm{T} \rightarrow {}^{2}_{4}\mathrm{He}\ (3.5\ \mathrm{MeV}) + \mathrm{n}\ (14.1\ \mathrm{MeV}) \qquad (1.1) $$

seems to be the most promising one, due to its favorable cross-section. In the tokamak device, a doughnut-shape thermonuclear plasma is confined using a strong toroidal magnetic field induced by external coils and a poloidal magnetic field self-generated by the plasma current (see Fig. 1.1).

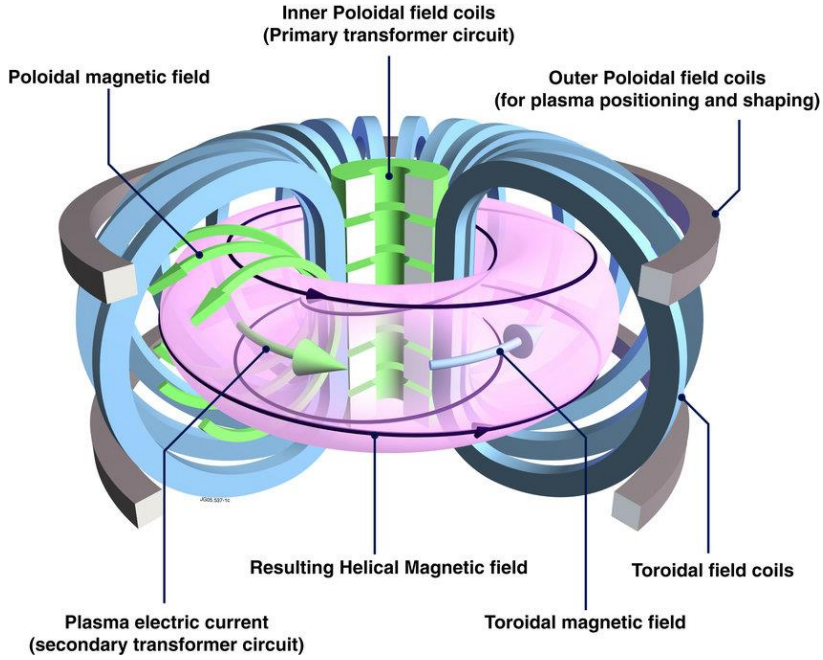


***Figure 1.1*** *Schematic view of the tokamak device.*

There are however several scientific and technological challenges on the way to construction of the fusion power plant. One of them is an efficient control of the plasma current profile to ensure stable steady-state plasma conditions. Among several techniques, the Lower Hybrid Current Drive (LHCD) is a key method to generate a continuous additional off-axis toroidal plasma current. It also allows a control of current profile by optimizing the power deposition

of the electromagnetic wave in the fusion plasma. However, during LHCD operation, a population of suprathermal electrons is generated in the plasma. Those electrons emit hard X-ray bremsstrahlung by Coulomb collision with ions of the plasma. Besides LHCD, a population of fast electrons – so-called runaway electrons – can also arise when the acceleration force (electric field) becomes greater than the friction force (Dreicer mechanism). These electrons can undergo a continuous acceleration and reach relativistic velocities. They pose a threat to the tokamak since they can potentially damage the first wall of the reactor and diagnostic systems.
Another issue originates from the fact that future fusion devices such as ITER will have to use heavy metallic elements like tungsten (W) as the plasma-facing components, in order to limit tritium retention. The heavy impurities generated by physical or chemical sputtering can then cool down the plasma and thus strongly degrade the fusion reaction by radiation emission in the soft X-ray (SXR) range. Therefore, efficient impurity mitigation methods must be developed and should include the effect of the heating systems such as Neutral Beam Injection (NBI) or Ion Cyclotron Resonance Frequency Heating (ICRH) on the impurity distribution. However, in case of LHCD the interaction between the induced energetic electron population and the heavy impurities remains unclear, while it could compromise both the control of the current profile and the mitigation of impurity accumulation in future fusion reactors. The Tore Supra tokamak recently upgraded to WEST - W Environment in Steady-State Tokamak - is a unique device to perform such studies in ITER-relevant plasma conditions.

The main objective of this project is to investigate the interplay between heavy impurity transport and the shape of the LHCD power deposition. For this purpose, the experimental data from WEST tokamak (see Sec. 3.1) are used. Such an investigation also requires computational work in order to create an accurate description of the Coulomb collisions of electrons with high-Z impurities in the plasma and modeling of emitted bremsstrahlung. The considered physical model should include the effects of partial screening occurring during the interaction of suprathermal electrons and high-Z ions.

Plasma X-ray emissivity measurements and subsequent tomographic reconstructions of plasma emissivity help to study simultaneously the energetic electrons and heavy impurities behavior. These kinds of measurements allow inference on the interaction mechanisms between these two populations. An important part of the project is a computational work performed with the dedicated numerical codes (see Sec. 3.2) to simulate the Lower Hybrid wave propagation and absorption in the plasma and to understand the interplay between energetic electrons and impurities. The results obtained in the framework of the proposed project will help to choose efficient methods of control of the plasma current profile and impurity mitigation techniques in magnetic confinement devices. These topics play a crucial role for the development of methods for plasma control in the International Thermonuclear Experimental Reactor ITER.

## 2. State of the art

The continuous operation of fusion reactors based on a magnetic confinement plasma system such as tokamak devices requires to provide continuously the adequate toroidal plasma current. In case of conventional systems with short pulsed plasma discharges, the plasma current is induced by a time-varying magnetic field produced by the central solenoid (cf. Fig 1). A variety of methods have been proposed to provide continuous current such as neutral beam injection (NBI) or radio-frequency waves in several frequency ranges. In the next decades, achieving and controlling steady state fusion plasmas will be one of the major challenges for tokamak physics. During the last years, studies have been performed to identify efficient non-inductive methods for current drive and hence building the density profile of the toroidal current which flows in the tokamak plasma by launching an EM wave [Challis, 1989], [Tanaka, 1991], [Oikawa, 2000], [Peysson, 2000], [Raman, 2001]. However, only few of the methods are attractive in terms of current drive efficiency and power deposition density [Fisch, 1987]. It seems that the most promising experimental results in fusion reactor relevant conditions have been obtained by current drive induced by LH wave with electrostatic polarization [X. Garbet, 1994]. The LH wave, due to the Landau damping, drives a high parallel momentum to electrons along the toroidal magnetic field direction and a net plasma current may be driven. An efficient and relatively simple detection method of this process consists in registration of the non-thermal bremsstrahlung radiation in the hard X-ray (HXR) spectral range. The time resolved observation of the HXR emission profiles measured in the photon energy range of 20 keV – 200 keV can provide essential information about the temporal evolution of the current density profile.

The choice of relevant plasma-facing materials is also of critical importance for the performance of nuclear fusion devices. ITER will not be able to use traditional carbon composites as a plasma-facing material due to their high tritium retention and erosion rates. Tungsten (W) was selected instead for its lower tritium retention, low physical and chemical sputtering as well as good resilience to intense heat fluxes [Pitts 2019]. However, heavy non-fully ionized impurities such as tungsten represent a major issue for the tokamak performance. Indeed, heavy impurities accumulating in the core plasma can radiate a significant amount of energy in particular in the SXR range, cooling down the plasma. This phenomenon can lead to radiative collapses and even to the plasma termination (disruption). Thus, tungsten concentration should be kept under tolerable levels – for instance $c_W = n_W/n_e < 10^{-4}$ for the ITER goal $Q = P_{fus}/P_{aux} \geq 10$ - to prevent unmanageable radiative cooling [Puetterich 2010]. It is therefore crucial to develop diagnostic tools to estimate - in real-time - the local impurity density in the plasma and to identify actuators, like localized Radio-Frequency heating, that can prevent or mitigate its central accumulation and keep the plasma under acceptable tungsten concentrations.

Besides, the impurity distribution can exhibit poloidal asymmetries, in particular due to the heating systems. For instance, it has been shown that NBI can induce Low-Field-Side (LFS) poloidal asymmetry due to the centrifugal force [Wesson 1997] while ICRH can affect the electrostatic potential leading to High-Field Side (HFS) accumulation [Bilato 2017]. These

poloidal asymmetries can significantly affect the radial transport of impurities [Angioni 2015]. Therefore, efficient heating scenarios minimizing the inward influx of tungsten impurities must be investigated with the help of robust and fast diagnostics and reconstruction methods. However, in case of LHCD the interaction between the power deposition profile and the distribution of heavy impurities remains poorly understood and is rarely reported in the scientific literature. On EAST tokamak, an experimental observation of the suppression of W accumulation induced by LHCD has recently been reported [Zhang 2017]. Additionally, an in-out impurity poloidal asymmetry in the presence of LHCD was observed in SXR signal for the first time on Tore Supra discharge #46564, during a W laser blow-off injection, but the understanding of this phenomenon still requires further theoretical and experimental investigations [Mazon 2012].

WEST - Tungsten (W) Environment in Steady State Tokamak – has been upgraded from Tore Supra and has started its operations with first plasmas in late 2017 [Johnston 2017]. Steady-state plasmas in X-point geometry of a few seconds duration were obtained in 2018 with a few megawatts of input power from LHCD and ICRH. Recently, the high confinement mode (H-mode) has been achieved at WEST. The LHCD system is an indispensable tool for achieving the goals of WEST in terms of long pulse operation, in particular the high fluence scenarios (up to 1000 s long pulses). The LHCD system has undergone a complete upgrade and will have a capability of 7 MW coupled to the plasma for up to 1000s. On the theoretical side, powerful numerical tools were developed in order to model the LH wave – plasma interaction in Tore Supra: a ray-tracing code C3PO is used to calculate the LH wave propagation in the plasma [Peysson 2012] and the LH wave absorption by electrons of the plasma is calculated thanks to the 3D bounce averaged relativistic Fokker-Planck solver LUKE [Peysson 2014]. The synthetic diagnostic R5-X2 [Peysson 2008] predicts the resulting fast electrons Bremsstrahlung radiation in the HXR range and can be compared with experimental measurements. Upgrading Tore Supra to WEST induced new challenges due to the inevitable presence of tungsten in the plasma. First of all, the fast electron collision operator in the numerical code must take into account screening effects with high-Z impurities. Moreover, different ionization states must be considered in the calculations of SXR and HXR emission. This requires an additional work on updating the existing numerical tools. So far, only low-Z fully stripped impurities (usually carbon) were considered in all kinetic calculations, thus an impurity transport code was not needed to evaluate the effective charge of ions in the plasma. However now, it becomes crucial to update the ray-tracing calculations (C3PO) and the LUKE kinetic code by including the calculation of all ionization states of the tungsten impurities, since it may change significantly the fast electron dynamics. This will be an important step for an accurate estimation of the LHCD efficiency, but also for the post-disruptive electron runaway dynamics [Hesslow 2017].

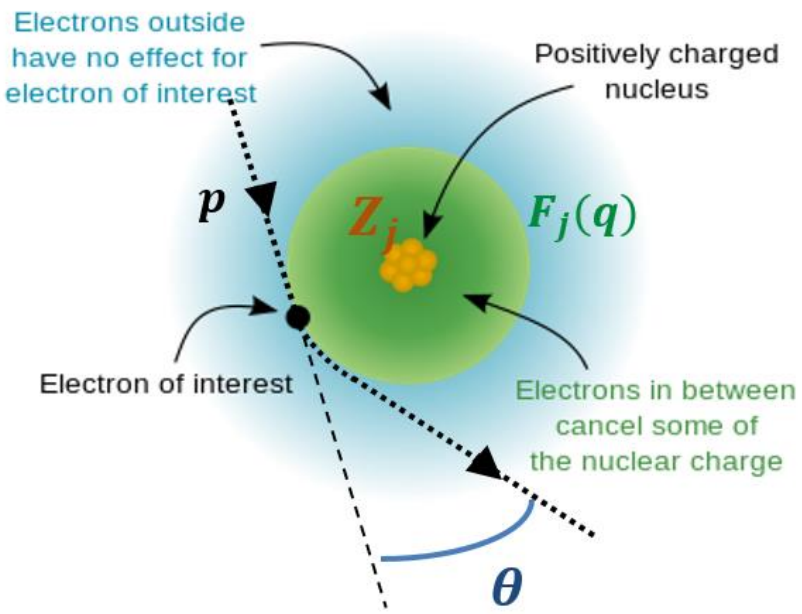


***Figure 2.1.*** *Representation of the partial screening effect occurring during a Coulomb collision between a partially ionized impurity atom and a free incident electron.*

The effective charge $Z$ of the impurity ion denoted, as seen by the fast incident electron, results from the screening of the nucleus charge $Z_j$ by the $N_{e,j}$ electrons bounded to the ion denoted $j$.

$$Z = Z_j - F_j(\vec{q}), \tag{2.1}$$

where $\vec{q} = \frac{2\vec{p}}{\alpha} sin\left(\frac{\theta}{2}\right)$ is the momentum transfer in the scattering process (in the first Born Approximation), with $\vec{p}$ the electron momentum, $\theta$ its deflection angle and $\alpha \simeq 1/137$ the fine-structure constant. The atomic form factor $F_j(\vec{q})$ corresponds to the Fourier transform of the electron density distribution $\rho_j(\vec{r})$ in the momentum space:

$$F_j(\vec{q}) = \int \rho_j(\vec{r}) e^{-i\vec{q}\cdot\vec{r}/a_0} d^3\vec{r}, \tag{2.2}$$

with $N_{e,j} = \int \rho_j(\vec{r}) d^3\vec{r}$ the total number of bound electrons. In the subsequent part of the report, we use the spherically averaged electron density defined as: $\tilde{\rho}_j(\mathrm{r}) = \frac{1}{4\pi}\int_0^{\pi}\int_0^{2\pi} \rho_j(\vec{r}) sin\theta d\theta d\phi$. Thus, the form factor expression simplifies to:

$$F_j(q) = 4\pi \int_0^{+\infty} \tilde{\rho}_j(r) \frac{r a_0}{q} \sin(qr/a_0)\, dr. \tag{2.3}$$

It naturally follows from the form factor definition that the condition $0 \leq F_j(q) \leq N_{e,j}$ must be fulfilled. The limit case $F_j(q) \to N_{e,j}$ is referred to as *full screening* or *complete screening*, while $F_j(q) \to 0$ is referred to as the *no screening* or *zero screening* case.

Finding the correct expression of the atomic form factor will allow describing the partial screening effect and assessing correctly the Coulomb collisions between fast electrons and heavy impurity ions. Calculations of the atomic form factor based on the Thomas-Fermi model of the ion have been reported in [Kirillov 1975]. More recently, the partial screening effect was taken into account for cold post-disruptive tokamak plasmas and impurities with medium-Z such as Argon, in order to study the dynamics of runaway electrons [Hesslow 2017, 2018]. One of the goals of this project is to extend the study to regular steady-state tokamak plasmas with core temperatures $T \geq 1keV$ and from low-Z to high-Z impurities, with a focus on tungsten ions. In particular, the partial screening effect could impact the LHCD efficiency and the fast electron Bremsstrahlung in the presence of W impurities in the plasma. The preliminary theoretical investigations on this topic are reported in Section 4.

The measurement of plasma X-ray emissivity has been carried out at several tokamak devices such as JET [Granetz 1988], [Ingesson 1998], Tore Supra [Peysson 2001], [Mazon 2012], TCV [Anton 1996], COMPASS [Mlynar 2012]. The reconstruction of the local plasma emissivity in a poloidal cross-section by 2D tomography is a very challenging task. This is due to the ill-posed nature of the inversion problem, with very sparse line-integrated measurements due to the lack of accessibility of the vacuum vessel and the presence of noise in the measurements. Several tomography methods have been developed so far to find the optimal solution of this problem. A hybrid pixel/analytic algorithm based on a poloidal Fourier analysis and a radial Abel inversion was presented in [Granetz 1988]. A constrained optimization method that uses anisotropic smoothness on magnetic flux surfaces as an objective function was applied in [Ingesson 1998]. The applicability of the minimum Fisher information method was tested for neutron emissivity reconstruction in [Anton 1996]. In addition, a comparative study concerning four methods (maximum likelihood, maximum entropy, Phillips-Tikhonov regularization and a Monte Carlo back-projection algorithm) and their applicability to plasma tomography on JET tokamak is reported in [Craciunescu 2009]. More recently, several original methods with promising results were developed by both our teams, based on an upgraded Minimum Fisher Information method [Jardin 2016a], a genetic algorithm [Bielecki 2018a] and a Monte-Carlo [Bielecki 2018b] approach, as well as neural networks [Jardin 2018] in the prospect of real-time impurity control. WEST will be thus the ideal platform to test, validate and benchmark these innovative tomography methods.

# 3. Research methods

## 3.1 West tokamak, SXR / HXR diagnostics, LHCD system and tungsten walls

### 3.1.1 The Tore Supra / WEST tokamak

Tore Supra, being equipped with superconducting coils [Turck 1987], tackled one of the most critical issues on the way to a fusion reactor based on the tokamak concept: steady-state operation. Consequently, the tokamak is equipped with various high power wave heating and current drive systems (*i.e.* Lower Hybrid Current Drive (LHCD), Ion Cyclotron Resonance Heating (ICRH), Electron Cyclotron Resonance Heating (ECRH)) that makes it a unique experimental platform to study of the suprathermal electron population behavior and advanced scenarios with ITER relevant density of the plasma [Belo 2005].

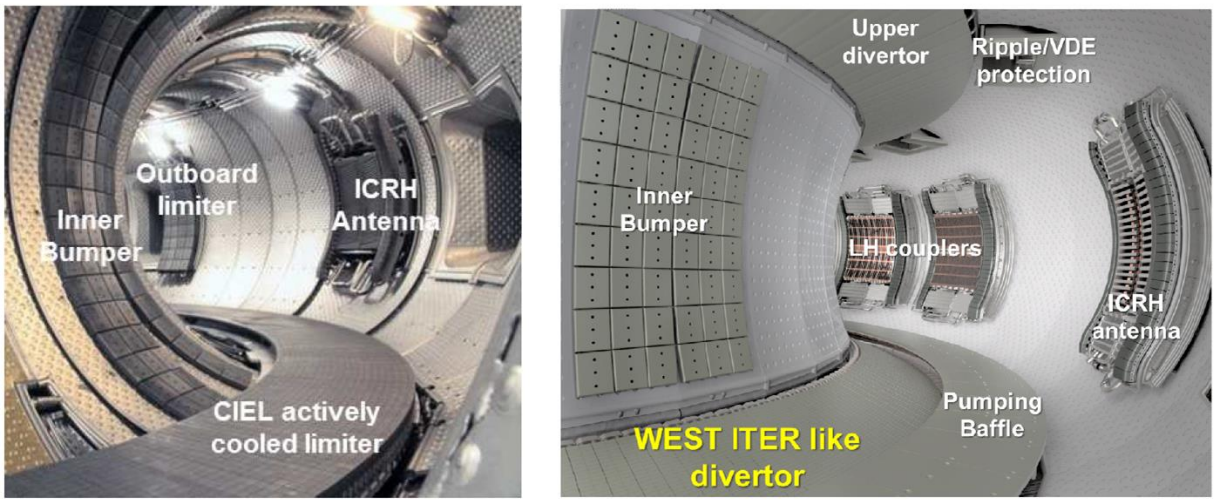


***Figure 3.1.*** *Transition from the Tore Supra tokamak (left) to WEST (right) [Ghendrih 2015].*

WEST was upgraded from Tore Supra, see Figure 3.1, started its operations in late 2017 [Johnston 2017] and achieved steady-state plasmas in X-point geometry of a few seconds duration and few megawatts of input power in 2018. The LHCD system has undergone a complete upgrade and will have a capability of 7 MW coupled to the plasma for up to 1000s.

### 3.1.2 Hard and Soft X-Ray detection systems

The experimental setup for soft X-ray measurements at Tore Supra uses 45 viewing lines in a horizontally oriented fan and 37 in a vertical fan providing poloidal resolution of about 3 cm together with toroidal beam width of about 12 cm in the center on the poloidal cross section (see Figure 3.2). It records the line-integrated SXR emission between 3 keV - 25 keV using silicon diode detectors. Application of two cameras: horizontal and vertical, with almost perpendicular fields of view, should make the reconstruction of the SXR emissivity in a poloidal cross-section of the plasma in Tore Supra tokamak possible. This is a crucial issue for the project realization. However, in practice, the very limited number of views causes the reconstruction to be a mathematical ill-posed problem. It is then a very challenging task to

obtain reliable results of the reconstruction. For this reason, algorithms that include additional *a priori* knowledge on the plasma conditions should be developed.

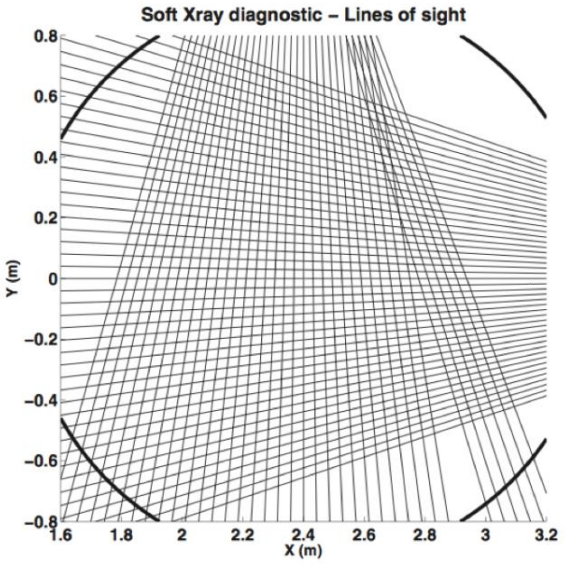


***Figure 3.2*** *Poloidal cross-section of the Tore Supra tokamak showing the lines of sight of the SXR tomographic system [Mazon 2012].*

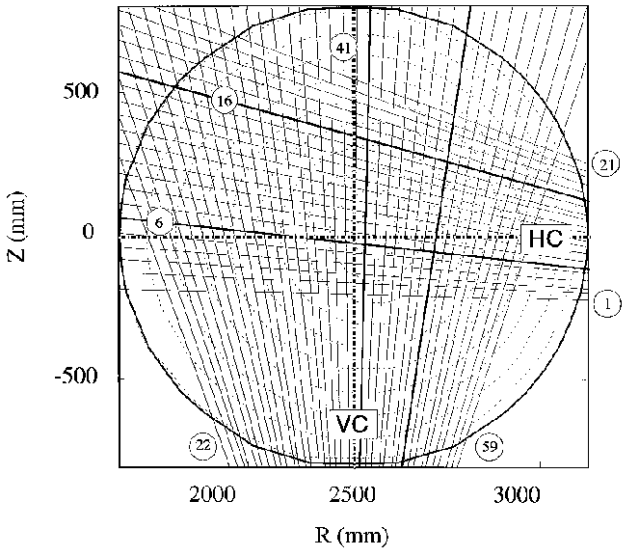


***Figure 3.3.*** *Poloidal cross-section of the Tore Supra tokamak showing the lines of sight of the HXR diagnostic [Peysson 2001].*

The tomography of the HXR bremsstrahlung emission is carried out on Tore Supra by two independent cameras as shown in Figure 3.3. The horizontal camera has 21 detectors, while the vertical one is composed of 38 detectors. The use of two distinct cameras enhances the spatial redundancy of the HXR measurements by covering the plasma poloidal cross-section with lines of sight of various inclinations, which is favorable for accurate emission profile reconstructions of noisy data. Even though they have a different number of detectors, both cameras are designed with similar geometrical and technical characteristics, in order to minimize uncertainties in the analysis.

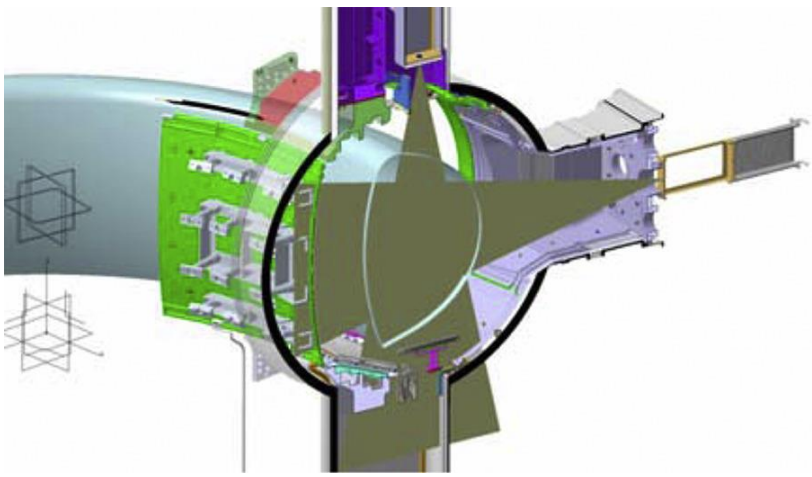

***Figure 3.4.*** *Spatial coverage of the WEST SXR tomographic system based on GEM detectors. The vertical camera is inside the vertical port [Mazon 2015].*

The WEST version is made of an array of a 75 pixels GEM detector located inside the vertical port so as to have a full view of the plasma, as depicted in Figure 3.4. A second GEM-based camera is proposed for the horizontal port with 128 detectors. Spatial resolution is about *1 cm* (viewing zone for horizontal GEM: *Z = +/-0.49 m* at *R = 2.54 m* and for vertical GEM: *R = [2.3 m to 2.78 m]* at *Z = 0*). Temporal resolution is performed simultaneously (2 signals), one slow at 1 kHz for transport studies application and one fast at *10 kHz* for MHD analysis, both being made available in real time during all pulse duration. The plasma local emissivity can be estimated by tomographic reconstruction. Then, based on this reconstruction, estimates of photon temperature and impurity distribution can be inferred.

The superior feature of GEM detectors over classical diodes is the capability to perform photon counting (each photon impinging on the detector is characterized in time, energy and position). It is thus possible to acquire spectra and to perform discrimination in energy (number of counts in a given energy range). A review of the GEM diagnostic possibilities for WEST can be found in [Mazon 2017] and [Jardin 2017].

### 3.2 X-ray reconstruction methods

**Hard X-ray diagnostics for LHCD.** The fast electron population is generated via electron Landau damping during the EM wave absorption. Fast electrons collide with ions or bulk electrons and radiate in the HXR spectral range, typically 20 keV - 200 keV. It means that the local HXR emissivity changes with the local EM wave power deposition. In order to obtain the emissivity distribution experimentally in the WEST plasmas, the line-integrated spectra is inverted by a tomographic method, typically by Abel inversion for HXR. Then, the obtained emissivity can be compared with the emissivity model constructed using numerical calculations. The Fokker-Planck solver (LUKE) is used to calculate the electron velocity distribution function for a given plasma configuration and heating scenario. Based on LUKE calculations, the required line-integrated spectrum is calculated with the synthetic diagnostic R5-X2 [Peysson 2008] taking into account the bremsstrahlung emission cross-section, viewing geometry, detector response function and present absorbers.

**SXR diagnostics for impurity studies.** The SXR plasma emissivity - as seen by a detector with spectral response $\eta(h\nu)$ and reconstructed by tomographic inversion - is expressed as the contribution of all ion species $S$ inside the plasma, as follows:

$$\varepsilon_{SXR}^{\eta} = n_e^2 \sum_S c_S . L_S^{\eta}(T_e, f_{S,q\in[\![0,Z_S]\!]}), \tag{3.1}$$

with $n_e$ and $T_e$ the electron density and temperature, respectively, the concentration $c_S = n_S/n_e$ and where $L_S^{\eta}$ denotes the filtered cooling factor of $S$ (in W.m$^3$) and $f_{S,q}$ the fractional abundance of the *q-th* ionization state of $S$. The cooling factor can be decomposed in the free-free (Bremsstrahlung), free-bound (recombination) and bound-bound (line radiation) contributions:

$$L_S^{\eta}(T_e) = \sum_{q=0}^{Z_S} f_{S,q}(T_e).\left[K_{S,q}^{\eta,ff}(T_e) + K_{S,q}^{\eta,fb}(T_e) + K_{S,q}^{\eta,bb}(T_e)\right], \tag{3.2}$$

neglecting here the transport effects on $f_{S,q}$. In the case of SXR plasma radiation dominated by tungsten impurities (usually valid for $c_W > 10^{-5} - 10^{-4}$), it is then straightforward to estimate the 2D map of the tungsten concentration from the following expression, where the cooling factor of the main hydrogenic species is easily calculated (Bremsstrahlung only) from the electron temperature profile:

$$c_W \simeq \frac{\varepsilon_{SXR}^{\eta} - n_e^2 L_H^{\eta}(T_e)}{n_e^2 L_W^{\eta}(T_e)}, \tag{3.3}$$

where $L_W^{\eta}$ is estimated thanks to detailed spectral atomic data provided by the ADAS project [ADAS], [Puetterich 2010], [Jardin 2017].

**Tomographic inversion methods.** The tomographic inversion problem consists in estimating the local emissivity field in a poloidal (i.e. vertical) cross-section of the plasma using sparse line-integrated measurements from one or several cameras. The geometry of the soft X-ray (SXR) diagnostic of Tore Supra [Mazon 2013] is depicted in Fig. 3.5 (left).

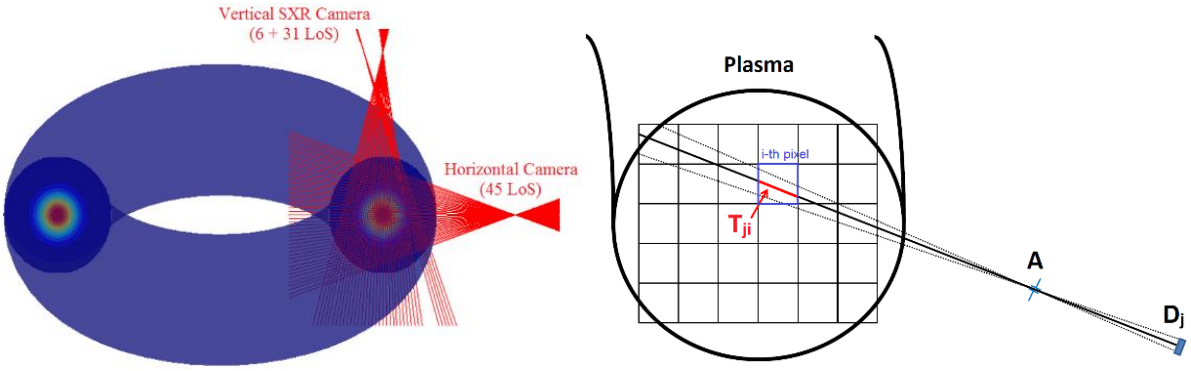


***Figure 3.5.*** *Left: Geometry of the soft X-ray diagnostic of the Tore Supra tokamak. Right: Layout of tokamak plasma 2D tomography: spatial discretization of the plasma in emissivity pixels in the poloidal cross-section defined by the detector-aperture system of the soft X-ray cameras.*

In the Line-of-Sight (LoS) approximation, the measurements $m_j$ of the *j-th* detector $D_j$ (in W.m$^{-2}$) looking at the plasma through the aperture A, as depicted in Fig. 3.5 (right), is given by the line integral:

$$m_j = \phi_j / E_j = \int_{LoS} \varepsilon^{\eta}(x,y) dr_j, \tag{3.4}$$

where $\phi_j$ is the incident photon flux onto the detector effective area (in W), $E_j$ is the geometrical étendue of the detector-aperture system (in m$^2$) and $\varepsilon^{\eta}(x,y)$ denotes the local plasma emissivity (in W.m$^{-3}$) filtered by the spectral response of the diagnostic. The

tomographic inversion problem can be written in mathematical term, after spatial discretization of the plasma in emissivity pixels:

$$\vec{m} = \bar{\bar{T}}.\vec{\varepsilon} + \vec{\xi}, \tag{3.5}$$

where the transfer matrix element $T_{ji}$ contains the length of the *j-th* LoS in the *i-th* pixel and $\vec{\xi}$ denotes systematic and statistical errors (*e.g.* electronic noise) in the measurements.

Unfortunately, the inversion problem is mathematically ill-posed with very sparse data set due to lack of accessibility in the tokamak and presence of noise in the measurements, i.e. the system of equations (3.5) is strongly underdetermined. Therefore a simple $\chi^2 = \left\|\vec{m} - \bar{\bar{T}}.\vec{\varepsilon}\right\|^2$ minimization is not applicable and some additional a priori information about the emissivity distribution is required to find a physically meaningful solution. Several methods for plasma tomography have been developed so far. X-ray emissivity reconstruction based on Abel inversion is a quite commonly used technique [Guosheng 2007]. The disadvantage of the method is the necessity to assume some symmetry of the reconstructed emissivity. Experimental evidences as well as theoretical predictions indicate though that poloidal asymmetries exist in the HXR emissivity and motivate the development of new tomographic methods and spectroscopic HXR systems to investigate the full two-dimensional emissivity distribution in a poloidal plane. Some other methods include post-processing of the obtained solution in order to impose the physical constrains on magnetic configuration etc. [Craciunescu 2008]. A comparative study concerning four methods (maximum likelihood, maximum entropy, Phillips-Tikhonov regularization and a Monte Carlo back-projection algorithm) and their applicability to the emission tomography reconstruction is reported in [Craciunescu 2009]. Nowadays, the Tikhonov regularization is the standard way of solving the inversion problem by finding the minimum of the following functional:

$$\vec{\varepsilon}_0 = arg\,\min_{\vec{\varepsilon}}\left(\chi^2 + \lambda.{}^t\vec{\varepsilon}.\bar{\bar{H}}.\vec{\varepsilon}\right), \tag{3.6}$$

where the regularization parameter $\lambda$ acts as a balance between overfitting of the measurements and regularization of the solution, i.e. smoothness of the reconstructed emissivity profile. For a given $\lambda$ value adequately chosen [Jardin 2016b], the inversion problem has now one unique solution:

$$\vec{\varepsilon}_0 = \left({}^t\bar{\bar{T}}.\bar{\bar{T}} + \lambda.\bar{\bar{H}}\right)^{-1}.{}^t\bar{\bar{T}}.\vec{m}. \tag{3.7}$$

The minimum Fisher information (MFI) method is the most commonly used in current tokamaks like TCV [Anton 1996], ASDEX Upgrade [Odstrcil 2016], Tore Supra [Mazon 2013], WEST [Jardin 2016a] or COMPASS [Imrisek 2016], associated with the following regularization operator:

$$\bar{\bar{H}}_{MFI} = (1-\tau)^t\bar{\bar{\nabla}}_X.\bar{\bar{W}}.\bar{\bar{\nabla}}_X + \tau^t\bar{\bar{\nabla}}_Y.\bar{\bar{W}}.\bar{\bar{\nabla}}_Y, \tag{3.8}$$

where $\overline{\overline{W}}$ denotes a ponderation matrix that imposes less constraint in the high emissivity region and where the spatial gradient $\overline{\overline{\nabla}}$ is often decomposed in the directions parallel (X) and perpendicular (Y) to the magnetic flux surfaces, with a preferential smoothing $0 < \tau < 0.5$ to account for the faster particle transport in the parallel direction.

Recent papers by our teams investigate new approaches to solve the inversion task: a genetic algorithm developed in [Bielecki 2018a] and a Monte-Carlo approach in [Bielecki 2018b] to optimize the minimum of the considered objective functional, as well as the use of neural networks coupled with large learning databases to perform tomographic reconstructions with real-time capabilities [Jardin 2018], as depicted in Figure 3.6.

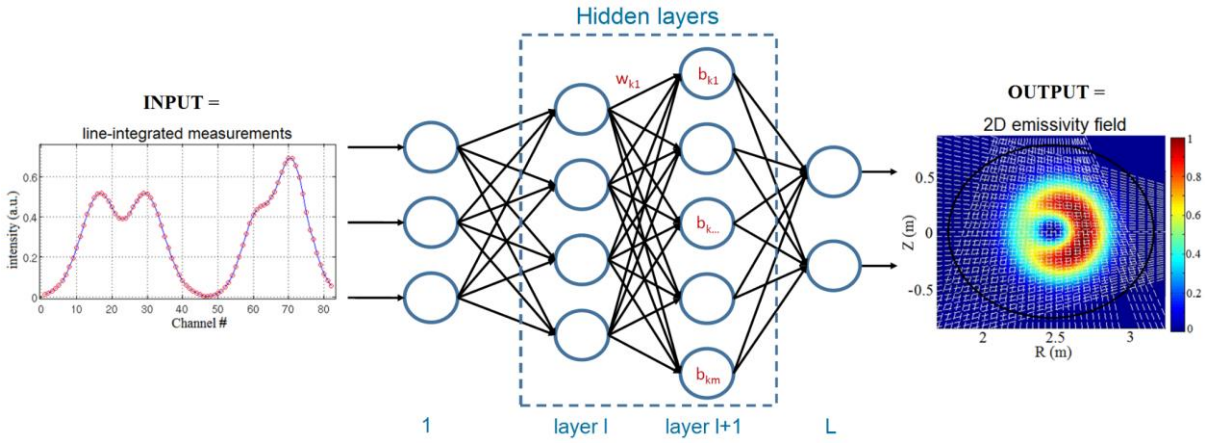


***Figure 3.6.*** *Layout of the neural network adapted to the SXR geometry of Tore Supra [Jardin 2018].*

## 3.2 Numerical tools to assess fast electron dynamics and plasma wave interaction

The current drive efficiency and the detailed behavior of the electron distribution function during EM resonance heating is well reproduced by Fokker–Planck codes, both in steady-state and in transient regimes [Peysson 1999], [Bernabai 1997]. It is widely recognized that the current profile control in non-inductively driven discharges will generally require more than a single current drive method. Therefore, complex plasma heating scenarios have been proposed to combine the various current sources into a smooth, MHD-stable current density profile in next-step fusion devices. To this end, some advantage could be taken from synergy effects due to the simultaneous use of different waves, as predicted, *e.g.* for LH and Electron Cyclotron waves, by kinetic simulation [Fidone 1984], [Giruzzi 1989]. In this case, the use of a 2D Fokker – Planck code to correctly describe the current drive process is necessary, owing both to the intrinsically 2D phenomena involved (*i.e.* parallel and perpendicular diffusion for lower hybrid and electron cyclotron waves, respectively) and to the nonlinear nature of the synergy effect.

We will start with a Maxwellian distribution function and solve the Fokker-Planck equation obtained from the quasilinear theory. If we take into account: i) collisions, ii) lower hybrid

waves and iii) particle transport the Fokker-Planck equation can be written symbolically as follows:

$$\partial_\tau f = (\partial_\tau f)_{LH} + (\partial_\tau f)_{COL} + (\partial_\tau f)_t, \tag{3.9}$$

where the subscripts in the right-hand side denote, from the left to the right, the effect of LH waves, collisions and particle transport. The function $f = f(u, \mu, s, \tau)$ is the electron distribution function, $\tau$ is the time normalized to the collision time, $u$ is the electron momentum normalized to the central thermal momentum at $\tau = 0$, $\mu = \cos\theta$ is the cosine of the pitch angle $\theta$ and $s = x/a$ is the normalized radial coordinate in the direction perpendicular to the ambient magnetic field $B_0$, supposed along the $z$ coordinate. The term related to LH wave may be given as follows:

$$(\partial_\tau f)_{LH} = \partial u_\parallel (D_{LH} \partial u_\parallel f), \tag{3.10}$$

where $D_{LH}$ is the diffusion coefficient in momentum space. Several solvers of the Fokker-Planck exist [Maj 2012], [Shoucri 1994], [Louche 1998]. However, the self-consistent modeling scheme of current profile control by radiofrequency waves should include the following issues:

1. A time-dependent kinetic equation to determine the driven current;
2. An appropriate model for the fast electron transport, integrated in the kinetic equation;
3. A one-dimensional macroscopic current diffusion equation, accounting for resistive effects and including the various current sources;
4. A set of 1D heat transport equations, with transport coefficients generally dependent on the current profile;
5. An appropriate model for the wave power deposition, fully consistent with current, temperature, and fast electron profiles.

On Tore Supra, a suite of modelling codes has been developed to assess LH wave propagation with the 3D ray-tracing code C3PO [Peysson 2012] and wave absorption by the plasma with the 3D bounce averaged relativistic Fokker-Planck solver LUKE [Peysson 2014] calculating the (suprathermal) energetic tail of the electron distribution function. The coupling of the LH wave between the radiative waveguide structure (LH launcher) and the plasma edge is estimated thanks to the ALOHA code (Advanced LOwer Hybrid Antenna) [Hillairet 2010]. A synthetic diagnostic R5-X2 [Peysson 2008] is used to predict the expected fast electron Bremsstrahlung (FEB) radiation in the Hard X-ray range and adjust iteratively the numerically estimated power deposition profile to the HXR experimental measurements. This numerical framework is interconnected with the integrated tokamak simulator code for global simulation of Tore Supra plasma discharges METIS for *Minute Embedded Tokamak Integrated Simulator* [Artaud 2018].

The ALOHA/C3PO/LUKE/R5-X2 codes form an integrated framework for LH wave – plasma interaction computation, as shown in Fig. 3.7.

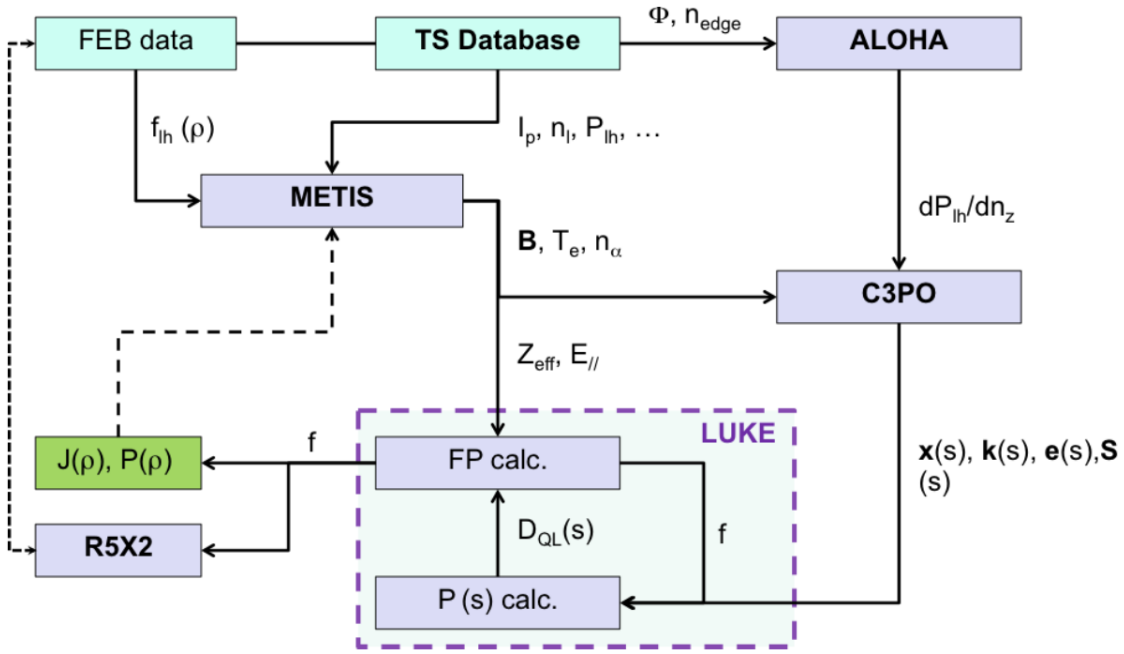


***Figure 3.7.*** *Work flow of the simulation routine for LH wave plasma – interaction, beginning from the Tore Supra database [Nilsson 2013].*

## 4. Works on extension of numerical models (partial screening, bremsstrahlung)

### 4.1 Calculation of the electron density distribution

The electron density $\rho(\vec{r})$ of an impurity atom can be calculated based on semi-classical methods (such as Thomas-Fermi (TF) model) or quantum-mechanical ab-initio calculations (Post Hartree-Fock (HF) methods, Density Functional Theory (DFT)). In the subsequent chapters the TF model, which can be considered as a precursor to modern DFT, is described, followed by a short introduction to DFT method. In the following subchapters the atomic units are used.

#### 4.1.1. Thomas-Fermi model

**Introduction to the model.** The TF model is a semi-empirical approximation for many-electron systems in an external potential $V(\vec{r})$. The model was developed in 1927 by Llewellyn Thomas and Enrico Fermi shortly after the introduction of the Schrödinger equation. The model is however based on the electron density $\rho(\vec{r})$, as a primary quantity, rather than the wave function (*cf.* Sec 4.1.3), thus it is known as a precursor to DFT. Due to semi-classical approximations, the model is not even able to reproduce some primary features of quantum mechanical systems such as shell structure in atoms. It is however still used in some modern applications due to its computational simplicity and the ability to extract qualitative trends analytically.

According to the model, the total energy of the system is given as the following functional of the electron density $\rho(\vec{r})$:

$$E[\rho(\vec{r})] = C_F \int \rho^{\frac{5}{3}}(\vec{r}) d^3\vec{r} + \frac{1}{2}\int \frac{\rho(\vec{r})\rho(\vec{r}')}{|\vec{r}-\vec{r}'|} d^3\vec{r} d^3\vec{r}' + \int V(\vec{r})\rho(\vec{r})\, d^3\vec{r}. \tag{4.1}$$

The last term in Eq. (4.1) describes the classical interaction with the external potential $V(\vec{r})$, the middle term is the classical Coulomb electron-electron interaction, while the first term describes kinetic energy of an electron gas within quantum homogenous electron gas approximation [Kim 1974] with the constant factor $C_F = \frac{3}{10}(3\pi^2)^{\frac{2}{3}}$. The electron density that minimizes $E[\rho(\vec{r})]$, subject to the constraint of keeping the number of electrons N constant i.e. $\int \rho(\vec{r}) d^3\vec{r} = N$, can be found using Lagrange multipliers technique:

$$\frac{\delta F[\rho(\vec{r})]}{\delta \rho(\vec{r})} = 0, \qquad F[\rho(\vec{r})] = E[\rho(\vec{r})] - \mu \int (\rho(\vec{r}) - N) d^3\vec{r}, \tag{4.2}$$

where $\mu$ is the Lagrange multiplier. This leads to the integral Thomas-Fermi equation for electron density:

$$\frac{5}{3} C_F \rho^{\frac{2}{3}}(\vec{r}) + V(\vec{r}) + \int \frac{\rho(\vec{r}')}{|\vec{r}-\vec{r}'|} d^3r' = \mu. \tag{4.3}$$

From Eq. (4.2), we can note that:

$$\frac{\delta E[\rho(\vec{r})]}{\delta \rho(\vec{r})} = \mu, \tag{4.4}$$

which gives the physical interpretation of the Lagrange multiplier μ as the chemical potential. The last term on the left-hand side of Eq. (4.3) can be treated as an induced potential associated to electron density $\rho(\vec{r})$:

$$\int \frac{\rho(\vec{r}')}{|\vec{r}-\vec{r}'|} d^3\vec{r}' = \tilde{V}(\vec{r}). \tag{4.5}$$

The electron density $\rho(\vec{r})$ and this induced potential $\tilde{V}(\vec{r})$ are related by the Poisson equation:

$$\nabla^2 \tilde{V}(\vec{r}) = 4\pi\rho(\vec{r}). \tag{4.6}$$

Using the above Poisson equation along with Eq. (4.3), we obtain the differential Thomas-Fermi equation for the induced potential $\tilde{V}(\vec{r})$:

$$\nabla^2 \tilde{V}(\vec{r}) = 4\pi \left(\frac{3}{5C_F}\right)^{\frac{3}{2}} \left(\mu - V(\vec{r}) + \tilde{V}(\vec{r})\right)^{\frac{3}{2}}. \tag{4.7}$$

Substituting $V_{eff}(\vec{r}) = V(\vec{r}) + \tilde{V}(\vec{r})$ to form the effective potential $V_{eff}(\vec{r})$, the above equation takes the following form:

$$\nabla^2\tilde{V}(\vec{r}) = 4\pi\left(\frac{3}{5C_F}\right)^{\frac{3}{2}}\left(\mu - V_{eff}(\vec{r})\right)^{\frac{3}{2}}. \tag{4.8}$$

Eq. (4.8) can be applied to a model of atom with atomic number Z. In this case:

$$V(\vec{r}) = -\frac{Z}{r}, \tag{4.9}$$

thus:

$$\nabla^2 V = -4\pi Z\delta(\vec{r}), \tag{4.10}$$

and

$$\nabla^2 V_{eff}(\vec{r}) = \nabla^2 V(\vec{r}) + \nabla^2\tilde{V}(\vec{r}) = -4\pi Z\delta(\vec{r}) + \nabla^2\tilde{V}(\vec{r}). \tag{4.11}$$

The chemical potential μ in Eq. (4.8) has obviously the constant value for any $\vec{r}$. In the special case of $\vec{r} \to \infty$: $\rho(\vec{r}) \to 0, V(\vec{r}) \to 0, \tilde{V}(\vec{r}) \to 0$ and since, cf. Eq. (4.3):

$$\rho(\vec{r}) = \left(\frac{3}{5\,C_F}\right)^{\frac{3}{2}}\left(\mu - V(\vec{r}) + \tilde{V}(\vec{r})\right)^{\frac{3}{2}}, \tag{4.12}$$

we obtain: $\mu = 0$ for $\vec{r} \to \infty$. Thus, $\mu = 0$ everywhere. Thus, for the Thomas-Fermi atom model, Eq (4.8) reduces to:

$$\nabla^2\tilde{V}(\vec{r}) = 4\pi\left(\frac{3}{5C_F}\right)^{\frac{3}{2}}\left(V_{eff}(\vec{r})\right)^{\frac{3}{2}}. \tag{4.13}$$

Combining the above equation with Eq. (4.11), we can write down the differential equation for the effective potential $V_{eff}(\vec{r})$:

$$\nabla^2 V_{eff}(\vec{r}) = 4\pi\left(\frac{3}{5C_F}\right)^{\frac{3}{2}}\left(V_{eff}(\vec{r})^{\frac{3}{2}} - Z\delta(\vec{r})\right). \tag{4.14}$$

For $\vec{r} \neq 0$:

$$\nabla^2 V_{eff}(\vec{r}) = 4\pi\left(\frac{3}{5C_F}\right)^{\frac{3}{2}}\left(V_{eff}(\vec{r})^{\frac{3}{2}}\right). \tag{4.15}$$

Assuming spherical symmetry, we can re-write the above equation in the spherical coordinates:

$$\frac{1}{r}\frac{d^2}{dr^2}rV_{eff}(r) = 4\pi\left(\frac{3}{5C_F}\right)^{\frac{3}{2}}\left(V_{eff}(\vec{r})^{\frac{3}{2}}\right). \tag{4.16}$$

Making the substitution:

$$V_{eff}(r) = -\frac{Z}{r}(\chi\alpha), \tag{4.17}$$

we can re-write Eq. (4.16) in the form of Universal Thomas-Fermi equation:

$$\frac{d^2\chi}{dx^2} = \frac{\chi^{\frac{3}{2}}}{\sqrt{x}}, \tag{4.18}$$

with boundary conditions: $\chi(0) = 1$ , $\chi(\infty) = 0$. Where: $r = \alpha x$, $x$ is dimensionless and $\alpha \approx 1.129\, Z^{\frac{1}{3}}$ is a constant of length dimension. The equation can be solved numerically while an approximate solution was given by [Fermi 1928].

**Numerical solutions of the TF equation.** Some analytical approximations of the solution of Eq. (4.18) have been developed, see *e.g.* [Csavinszky 1969]. It is nevertheless possible to estimate numerically the solution more accurately by using a Monte-Carlo approach. Starting from an initial guess $\chi^{(0)}(x) = 1/(1+2x)$ that matches basic properties of the solution, *i.e.* $\chi(0) = 1$ , $\chi(\infty) = 0$ and $\mathrm{d}^2\chi/\mathrm{dx}^2 > 0$ the following functional is minimized iteratively:

$$\chi^{(final)} = arg\min_{\chi}\left\|\frac{d^2\chi}{dx^2} - \frac{\chi^{\frac{3}{2}}}{\sqrt{x}}\right\|^2. \tag{4.19}$$

Since the calculations are limited, in practice the condition $\chi(\infty) = 0$ has to be changed for $\chi(x_{max}) = 0$ with $x_{max} \gg 0$. The solution of the Monte-Carlo approach is presented in Fig. 4.1, for $x_{max} = 100$ and $x_{max} = 1000$, showing a satisfying convergence of the iterative process and a good numerical accuracy for the typical range of interest $0 < x < 20$.

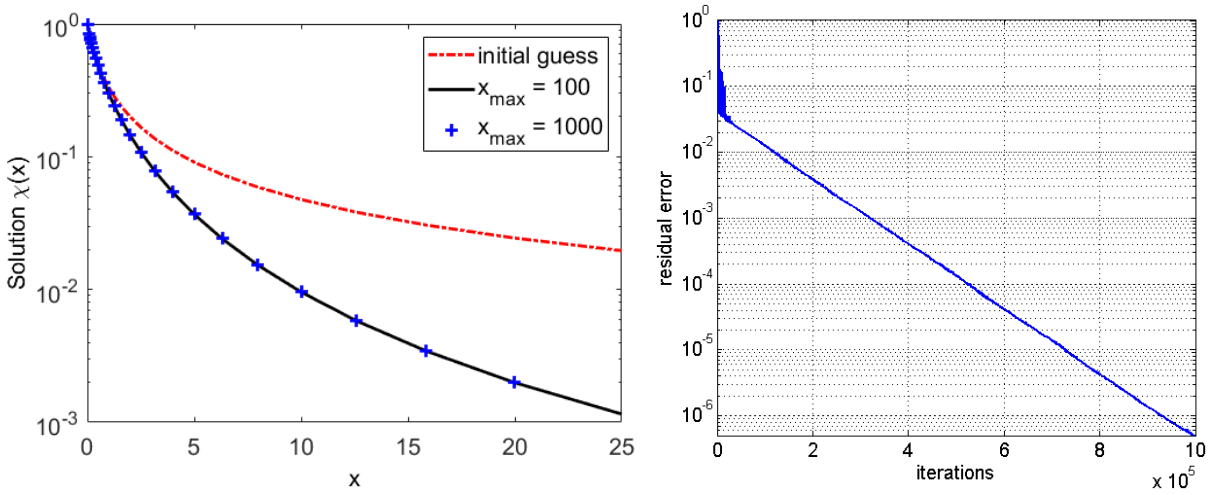


***Figure 4.1.*** *Left: numerical solution of universal TF equation for the neutral atom. Right: value of the residual error after n iterations.*

However, the above calculations apply only to neutral atoms, while positive ions have to be considered in the framework of this project. It is possibly to solve the TF equation for positive ions by adapting the boundary conditions: $\chi(0) = 1$, $\chi(x_0) = 0$ instead of $\chi(0) = 1$, $\chi(\infty) = 0$, as in the case of neutral atom [Lundqvist 1983]. The constant $x_0$ has a meaning of semi-classical radius of the ion. It corresponds to the fact that, for positive ions, the electron density vanishes for $x \geq x_0$ and thus $\chi(x \geq x_0) = 0$. The solution computed numerically for the case $x_0 = 7.5$ is shown on Fig. 4.2.

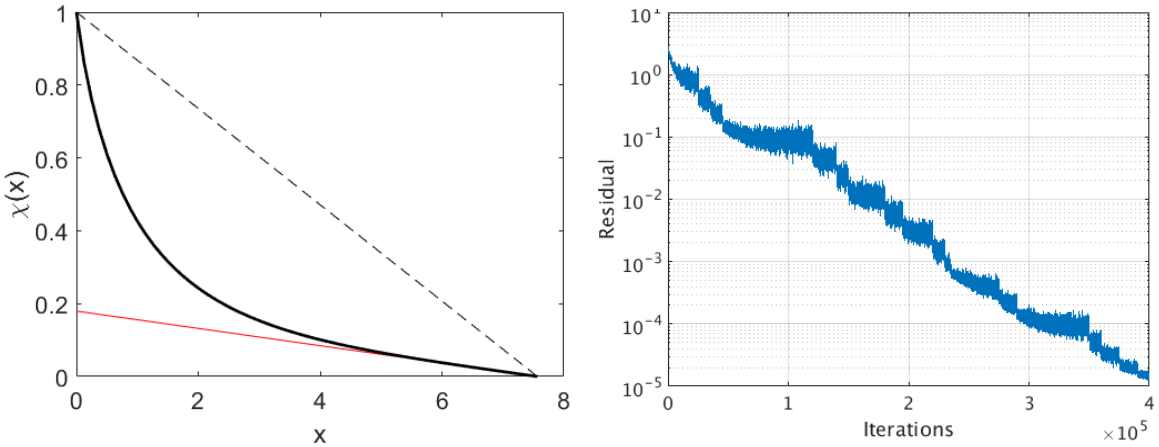


***Figure 4.2.*** *Left: numerical solution of universal TF equation for a positive ion with* $x_0 = 7.5$ *in black, where the dashed line is the initial guess and the red line is the slope at* $x = x_0$*, giving the value of* $Q$ *at* $x = 0$*. Right: value of the residual error after n iterations.*

The effective potential $V_{eff}(r)$ around the ion can then be determined from:

$$V_{eff}(r) = \begin{cases} -\frac{Z}{r}\chi(r\alpha) - \frac{Zq}{r_0} & if\ r \leq r_0 \\ -\frac{Zq}{r} & if\ r > r_0 \end{cases}, \tag{4.20}$$

where $V(r_0) = \mu = \frac{-(Z-N)e^2}{r_0}$. The resulting effective potential is presented on Fig. 4.3.

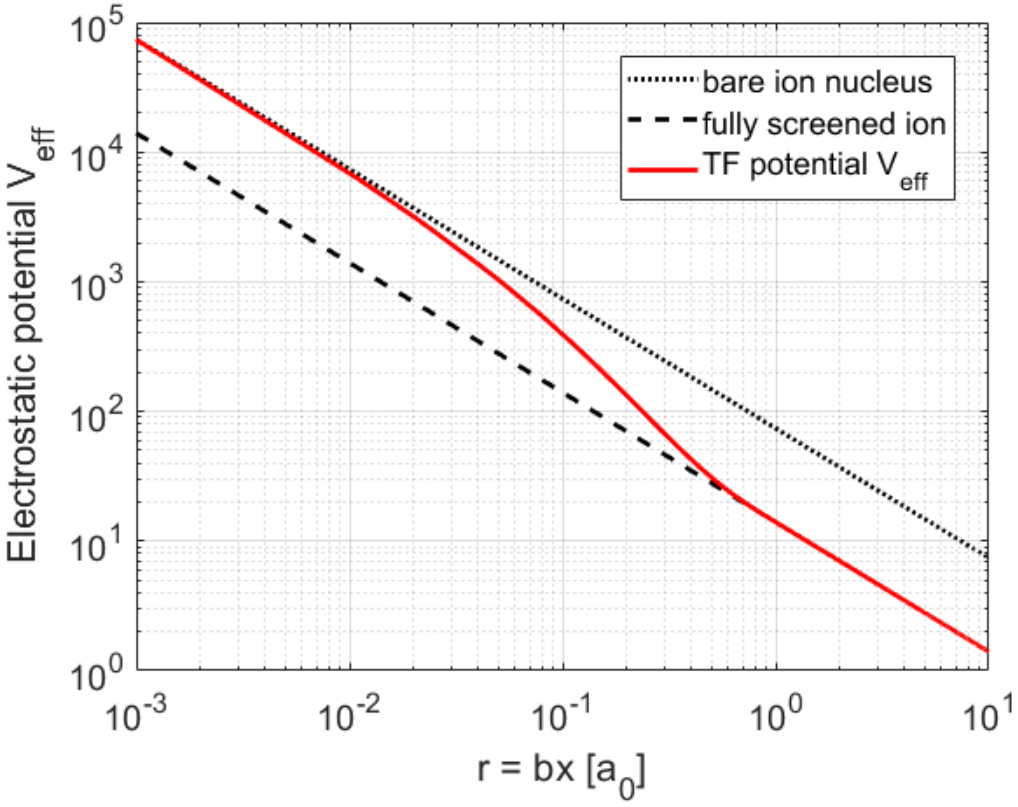


***Figure 4.3.*** *Effective potential around the ion as calculated from the solution of the TF equation.*

From Fig. 4.3, as expected, it can be seen that the effective TF electrostatic potential surrounding the ion nucleus is approaching the bare ion nucleus limit for low radius and the fully screened ion limit for radius above the typical ion size $r > 1$. Furthermore, applying the Gauss theorem at $x \geq x_0$ leads to the additional boundary condition:

$$-x_0 \frac{d\chi}{dx}(x_0) = 1 - \frac{N}{Z} = Q, \tag{4.21}$$

where $Q$ is the ionization degree of the considered ion. This mean that there is a one-to one relationship between the values of $x_0$ and $Q$. This relationship can be obtained by solving the TF equation for different values of $x_0$, as depicted in Fig. 4.4.

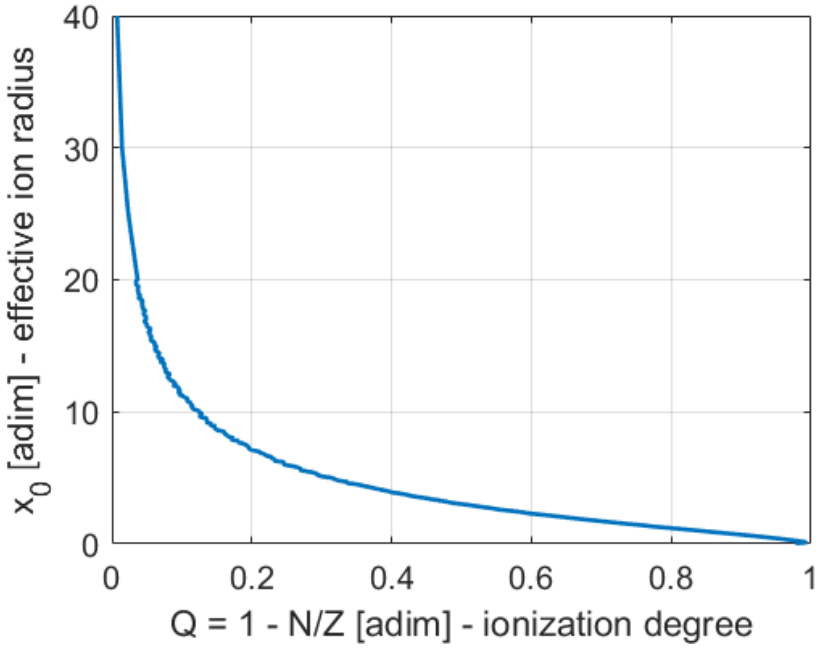


***Figure 4.4.*** *Dependency between the semi-classical radius $x_0$ and $Q = 1 - N/Z$.*

This curve can be used in practice, through interpolation, to determine the value of $x_0$ for any ionization degree $Q$. The electron density can be calculated from the electrostatic potential as follows [Lundqvist 1983]:

$$\rho(r) = \frac{8\pi}{3h^3}(2m)^{3/2}[\mu - V(r)]^{3/2}, \quad for\ \mu \geq V(r), \tag{4.22}$$

and the electron density vanishes outside of the ion $\rho(r \geq r_{max}) = 0$, for $\mu < V(r)$.

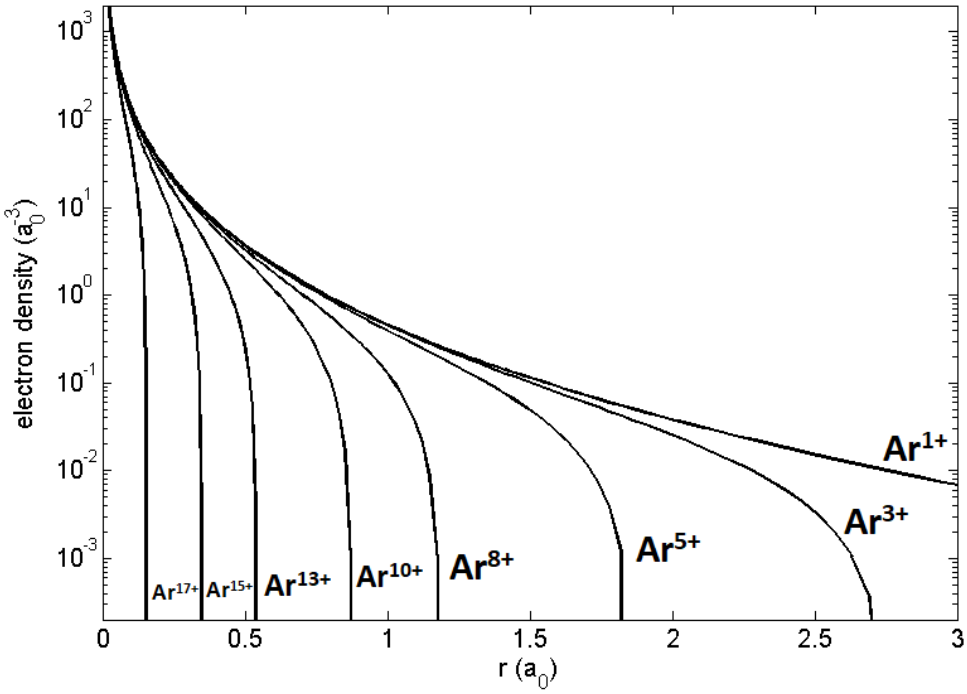


***Figure 4.5.*** *Electron density in Argon as calculated numerically from the TF model.*

It can be seen from Fig. 4.5 that, as expected, the TF model does not describe accurately the details of the electron shells. A more realistic approach based on the Density Functional Theory (DFT) can be used for this purpose.

As shown by [Kirillov 1975], the atomic form factor can be directly calculated from the solution of the universal TF equation:

$$F(q) = Z \int_0^{x_0} \chi^{3/2} \frac{sin\,\xi x}{\xi x} \sqrt{x}\, dx, \tag{4.23}$$

where $\xi = q a_{TF}$, $a_{TF} = a_0 (9\pi^2/128Z)^{1/3}$ and $x = r/a_{TF}$. The condition to recover the total number of bounded electrons is:

$$N_e = Z \int_0^{x_0} \chi^{3/2} \sqrt{x}\, dx. \tag{4.24}$$

In the limit $\xi x_0 \ll 1$ (low electron momentum), we have $sin(\xi x)/\xi x \simeq 1$ and thus $F(q) \simeq N_e$. For the opposite limit $\xi x_0 \gg 1$ (high electron momentum), we have $\chi \to 1$ and thus:

$$F_{\xi x_0 \gg 1}(q) \simeq Z \int_0^{x_0} \frac{sin\,\xi x}{\xi x} \sqrt{x}\, dx = \frac{Z}{\xi^{\frac{3}{2}}} \int_0^{x_0} sin\, y \frac{dy}{\sqrt{y}} = Z \sqrt{\frac{\pi}{2\xi^3}} = \frac{N_e}{t}, \tag{4.25}$$

with $t = (N_e/Z)\sqrt{2\xi^3/\pi}$. Kirillov proposed the following function to interpolate F(q) between these two limit cases:

$$F_j(q) = \frac{N_e}{1+t}. \tag{4.26}$$

It can be easily checked that $F_{\xi x_0 \gg 1}(q) \to N_e/t$ and $F_{\xi x_0 \ll 1}(q) \to N_e$. For convenience, the form factor can be reformulated as done in [Hesslow 2017]:

$$F_j(q) = \frac{N_{e,j}}{1 + \left(q a_j\right)^{3/2}}, \tag{4.27}$$

where the effective ion radius $a_j$ can be expressed as:

$$a_j = \frac{N_e^{2/3}}{Z} \frac{(9\pi)^{1/3}}{8} a_0. \tag{4.28}$$

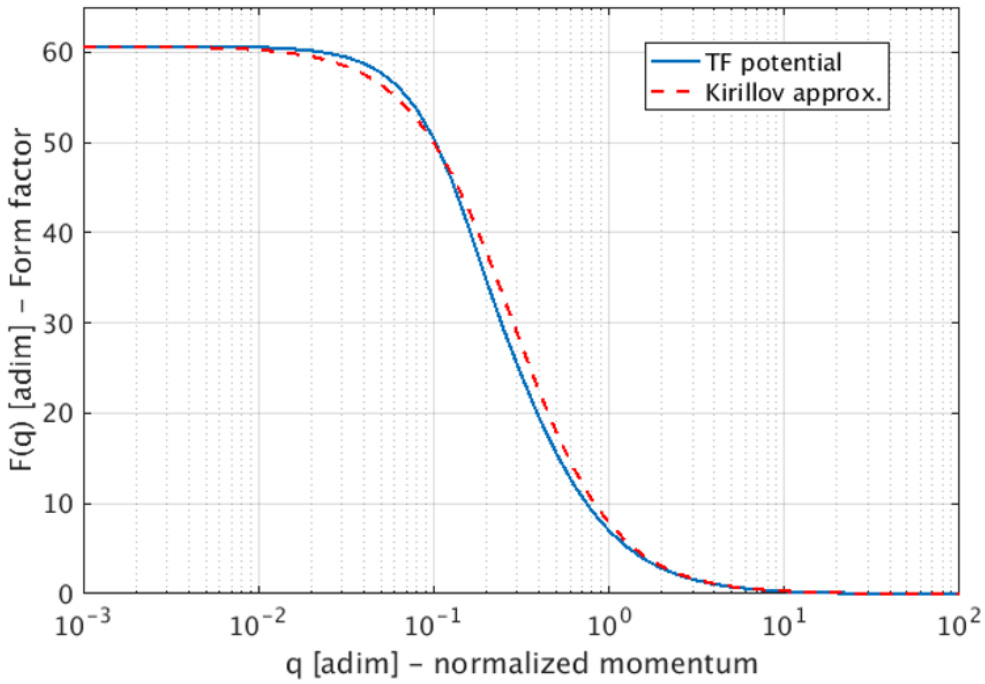


***Figure 4.6.*** *Atomic form factor of the tungsten ion $W^{14+}$ obtained from the TF model.*

### 4.1.2. Tseng-Pratt model (Yukawa potential)

An alternative method to derive an approximate analytical expression of the atomic form factor is based on the Yukawa potential, writing the electrostatic potential around the ion nucleus as the sum of the classical Coulomb term and an exponential term accounting for the screening of bounded electron at short distances from the nucleus [Pratt, Tseng 1972]:

$$V_{eff} \simeq \frac{1}{4\pi\varepsilon_0 r}[Z + (Z - Z_0)\, exp(-\lambda_0 r)], \tag{4.29}$$

where $\lambda_0$ is a constant. This approach is complementary to the Thomas-Fermi model, since it focuses on the region very close to the nucleus where the potential can be fitted by an exponential, while the accuracy of the Thomas-Fermi model increases with the number of bounded electrons. A more complete description of this model can be found in the calculation notes [Peysson 2019]. The electron density can then be obtained using the Poisson equation, in spherical coordinates:

$$\nabla^2 V = \frac{1}{r^2}\frac{\partial}{\partial r}\left(r^2 \frac{\partial V}{\partial r}\right) = -\frac{\rho(r)}{\varepsilon_0}. \tag{4.30}$$

Thus, the first term is:

$$r^2 \frac{\partial V}{\partial r} = -Vr - \lambda_0 \frac{r}{4\pi\varepsilon_0}(Z - Z_0)\, exp(-\lambda_0 r). \tag{4.31}$$

And then:

$$\begin{aligned} &\frac{1}{r^2}\frac{\partial}{\partial r}\left(r^2 \frac{\partial V}{\partial r}\right) = -\frac{1}{r^2}\left(V + r\frac{\partial V}{\partial r}\right) - \lambda_0 \frac{1}{4\pi\varepsilon_0 r^2}(Z - Z_0)[1 - \lambda_0 r]\, exp(-\lambda_0 r) \\ &= \frac{1}{r^3}\left(\lambda_0 \frac{r}{4\pi\varepsilon_0}(Z - Z_0)\, exp(-\lambda_0 r)\right) - \lambda_0 \frac{1}{4\pi\varepsilon_0 r^2}(Z - Z_0)[1 - \lambda_0 r]\, exp(-\lambda_0 r). \end{aligned} \tag{4.32}$$

And finally we can obtain the expression of the electron density:

$$\rho(r) = \frac{\lambda_0^2}{4\pi r}(Z - Z_0)\, exp(-\lambda_0 r). \tag{4.33}$$

It is then possible to estimate the atomic form factor based on Eq. (2.3):

$$F_j(q) = \frac{\lambda_0^2}{q}(Z - Z_0)\int_0^{+\infty} sin(qr)\, e^{-\lambda_0 r} dr. \tag{4.34}$$

Since the integral value is:

$$\int_0^{+\infty} sin(qr)\, e^{-\lambda_0 r} dr = \frac{q}{q^2 + \lambda_0^2}. \tag{4.35}$$

The calculations lead to the following expression of the form factor:

$$F_j(q) = \frac{N_{e,j}}{1 + \left(q a_j^{TP}\right)^2}, \tag{4.36}$$

wit$N_{e,j} = Z - Z_0$h and $a_j^{TP} = 1/\lambda_0$. An approximate analytical formula for the screening constant $\lambda_0$ can be found in [Lamoureux 1997], where it takes the expression:

$$\lambda_0^2 = 0.798Z \frac{1 - (Z_0/Z)^{n+1}}{1 - Z_0/Z} a_0^{-2} \tag{4.37}$$

with $n = Z(1/3 - 0.0020Z)$. An example of $\lambda_0$ values is shown on Figure 4.7, for all ionization stages of Argon (*Z=18*).

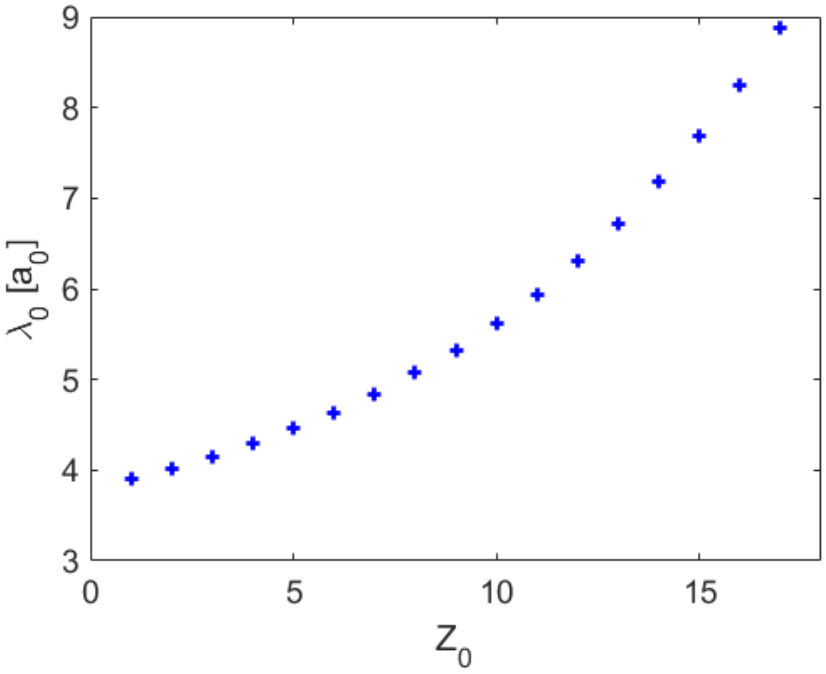


***Figure 4.7.*** *Values of the screening constant $\lambda_0$ for Argon (Z=18) and different ionization stages $Z_0$, as obtained from Eq. (4.37) and [Lamoureux 1997].*

It is then possible to estimate both the radial electron density, based on Eq. (4.33), and the atomic form factor based on Eq. (4.36). The corresponding electron density profile for all ionization stages of Argon is presented on Figure 4.8.

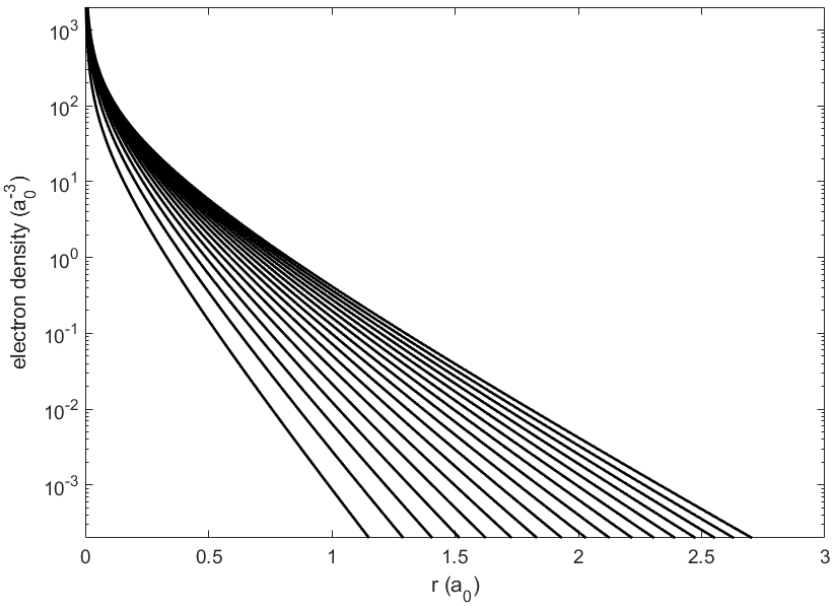


***Figure 4.8.*** *Radial electron density profile the different ionization stages of Argon (Z=18) according to the Tseng-Pratt model and screening constant $\lambda_0$ as in Eq. (4.37).*

### 4.1.3 Density Functional Theory (DFT)

DFT is a variational method that is presently one of the most successful and computationally efficient approaches to compute the electronic structure of matter. It is currently applied to

atoms [Gronowski 2017], molecules [Parr 1995], solids [Hasnip 2011], large molecular systems such DNA [Li 2001, Lipiec 2014] as well as to nuclei [Colo 2018]. The DFT relies on an idea to substitute the complicated many-body electron wave function, which is a function of *3N* variables (where N is the number of electrons), with the functional of electron density which contains only 3 variables and has an intuitive physical meaning. In this way it inherits from the presented TF model. Foundations for the DFT concept are given by two Hohenberg and Kohn (HK) theorem's [Hohenberg 1964]. The first HK theorem postulates that the ground state density $\rho_0(\vec{r})$ of a bound system of interacting electrons in some external potential $V(\vec{r})$ determines this potential uniquely. The second HK theorem states that an energy functional can be defined in terms of the electron density for the system, and further states that by taking the minimum of the energy functional according to the electron density, ground state energy can be found. These two theorems postulate that there exists one-to-one mapping relationship between electron density and system properties, but they do not provide any information on explicit form of this relationship. Practical way of solving many-electron problem within DFT formalism was given by Kohn and Sham [Kohn 1965]. They simplified the multi-electron problem into a problem of non-interaction electrons in an effective potential. This potential includes the external potential and the effects of the Coulomb interactions between the electrons, i.e., the exchange and correlation interactions. Since the exact form of exchange-correlation potential is not known, several approximations are commonly used. The simplest approximation - the Local-Density Approximation (LDA) - is based on an assumption that the density can be treated locally as a uniform electron gas *i.e.* the exchange-correlation energy at each point in the system is the same as that of a uniform electron gas of the same density. Because of this assumption LDA has a tendency to underestimate the exchange energy and to overestimate the correlation energy. To correct for this effect, functionals that include also the gradient of electron density have been proposed in order to account for the non-homogeneity of the true electron density. This approximation is referred to as Generalized Gradient Approximation (GGA). Further improvement was done in so-called Meta-GGA DFT functional where its form includes also the second derivative (the Laplacian) of the electron density. Difficulties in expressing the exchange part of the energy have driven the development of so-called hybrid functionals, where a component of the exchange energy calculated from the Hartree-Fock theory is included into the functional with the rest of exchange-correlation energy taken from other sources. One of the most commonly used hybrid functional is B3LYP, which stands for Becke, 3-parameter, Lee–Yang–Parr [Becke 1993]. In the presented studies the PBE0 hybrid functional was used. The PBE0 functional mixes the Perdew–Burke-Ernzerhof (PBE) exchange energy [Perdew 1996] with Hartree-Fock exchange energy in 3:1 ratio, along with the full PBE correlation energy:

$$E_{XC}{}^{PBE0} = \frac{1}{4} E_X{}^{HF} + \frac{3}{4} E_X{}^{PBE} + E_C{}^{PBE}, \tag{4.38}$$

where $E_X{}^{HF}$ is the Hartree–Fock exact exchange functional, $E_X{}^{PBE}$ is the PBE exchange functional, and $E_C{}^{PBE}$ is the PBE correlation functional. By transforming the interacting many body problem into the non-interacting system in an effective potential $V_{eff}(\vec{r})$, wavefunction can be easily represented by a Slater determinant of Kohn-Sham orbitals $\phi_i(\vec{r})$. The kinetic

energy functional of this system is exactly known. However, the exchange-correlation part of the total energy functional remains unknown. This scheme gives possibility to write down the one-electron Schrödinger-like equations (Kohn-Sham equations) of a fictitious system of non-interacting particles that generate the same density as the system of interacting particles:

$$\left(-\frac{\hbar^2}{2m}\nabla^2 + V_{eff}(\vec{r})\right)\phi_i(\vec{r}) = \varepsilon_i\phi_i(\vec{r}), \tag{4.39}$$

where $\varepsilon_i$ is the orbital energy of the corresponding Kohn-Sham orbitals $\phi_i(\vec{r})$ and the electron density on an N-electron system is:

$$\rho(\vec{r}) = \sum_{i=1}^{N} |\phi_i(\vec{r})|^2. \tag{4.40}$$

The effective KS potential is given as:

$$V_{eff}(\vec{r}) = V_{ext}(\vec{r}) + e^2 \int \frac{\rho(\vec{r}')}{|\vec{r} - \vec{r}'|}\overrightarrow{dr'} + \frac{\delta E_{XC}[\rho]}{\delta\rho(\vec{r})}, \tag{4.41}$$

where the last term defines exchange-correlation potential:

$$V_{XC}(\vec{r}) \equiv \frac{\delta E_{XC}[\rho]}{\delta\rho(\vec{r})}. \tag{4.42}$$

The KS equations (4.39) are self-consistent. To solve these equations, we start with an initial guess of the charge density $\rho(\vec{r})$. By using some approximate form for the functional dependence of the exchange-correlation energy $E_{XC}$ on density, we must compute $V_{XC}(\vec{r})$. The set of KS equations are then solved to obtain an initial set of KS orbital $\phi_i(\vec{r})$. This set of orbitals is then used to compute an improved density and the process is repeated iteratively until the density and exchange correlation energy converge, within some tolerance. In any practical application, the continuous problem given by KS equations (4.39) has to be mapped to a linear algebra problem that can be solved by a computer. This is done by representing the KS orbital $\phi_i(\vec{r})$ as a linear combination of basis functions:

$$\phi_i(\vec{r}) = \sum_{\alpha=1}^{N_{BF}} F_\alpha(\vec{r})C_{\alpha i}, \tag{4.43}$$

Where $F_\alpha(\vec{r})$ are the basis functions and $C_{\alpha i}$ are coefficients, *i.e.* numbers to be determined in the self-consistent calculations. Early in quantum chemistry, Slater Type Orbitals (STO) were used as basis functions because of their similarity with the solutions of the hydrogen atom. The Slater type orbitals have the following form in spherical coordinates:

$$S_\nu(\zeta, n, l, m, r, \theta, \phi) = \mathcal{N} r^{n-1} e^{-\zeta_\nu r} Y_{lm}(\theta, \phi), \tag{4.44}$$

where $\mathcal{N}$ is the normalization constant, and $Y_{lm}(\theta,\phi)$ are the spherical harmonic functions, *n*, *l*, and *m* are the principal, angular momentum, magnetic quantum numbers, respectively. Variable ζ is called the "exponent". The exponential dependence on distance reflects the exact form of the hydrogen-like orbitals. However, the calculation of the three- and four-center two-electron integrals with Slater orbitals is extremely slow and has no analytical form. Thus, for the practical reason, Gaussian functions are employed in the most of ab-initio codes. The two-electron integral can be much easier and faster computed when Gaussian functions are used (due to the Gaussian Product Theorem). Some numerical codes use Cartesian Gaussian Type Orbitals (GTO):

$$g_v(\vec{r}) = Nx^k y^m z^n e^{-\zeta_v \vec{r}^2} = Nx^k y^m z^n e^{-\zeta_v (x^2+y^2+z^2)}, \tag{4.45}$$

where *k*, *m*, *n* are not the quantum numbers but just parameters. While other codes use spherical GTO:

$$g_v(\vec{r}) = NY_{l,m}(\theta,\phi)r^l e^{-\zeta_v r^2} = NY_{l,m}(\theta,\phi)r^l e^{-\zeta_v (x^2+y^2+z^2)}. \tag{4.46}$$

The Gaussian functions given by Eq. (4.45) and (4.46) are called, in the quantum physics/chemistry community, primitive Gaussian functions. It is very common to group several primitive Gaussian functions to form a new Gaussian function called contracted Gaussian function:

$$G_\alpha(\vec{r}) = \sum_{v=1}^{N_\alpha} c_v g_v. \tag{4.47}$$

Contracting several primitive Gaussian functions into the contracted Gaussian, reduces computational effort, since the optimization of several coefficients can be performed in a single iteration. The further improvement and complication of basis functions is introduced by doubling all the basis functions to produce the double-zeta (DZ) type basis or to tripe all the basis functions to produce triple-zeta basis and so on. This kind of basis is referred, in general to as split-valence basis set. The further improvement can be achieved by introducing polarization and diffuse functions. In the presented calculation Relativistic Atomic Natural Orbitals (ANO-RCC) basis set was mostly exploited [Roos 2005]. This kind of basis set is obtained from correlated calculations (CASSCF/CASPT2 method) on atoms, thus it is especially adequate for correlated DFT calculations. Furthermore, since the presented study concerns mostly heavy elements such tungsten, relativistic effects are important. The theoretical basis for the relativistic quantum description is the Dirac one-electron equation with the Dirac four spinor $\psi$, which replaces the Schrödinger equation. Together with quantization of the electromagnetic field, this gives a quantum field theory – Quantum Electrodynamics (QED). However, for our application, it is enough to use approximate theories derived from QED, at the level of electrons described using self-consistent four-component orbitals with an added two-electron interaction. Furthermore, it is possible to simplify, with acceptable accuracy, the four-component formalism to a two-component

relativistic formalism, that can be implemented into the existing *ab initio* codes. There are several approaches to do that. In this study we used the Douglas-Kroll-Hess transformation [Douglas 1974, Hess 1985].

The one-electron Dirac-Hamiltonian in the standard representation is given by:

$$H_D = c\vec{\alpha} \cdot \vec{p} + \left(\beta - \boldsymbol{I}_{(4)}\right)mc^2 + V\boldsymbol{I}_{(4)}, \tag{4.48}$$

where $\vec{\alpha}$ is a 3-vector, whose components are constructed from the Pauli spin matrices and $\beta$ represents the following 4×4 diagonal matrix:

$$\beta = \begin{bmatrix} 1 & 0 & 0 & 0 \\ 0 & 1 & 0 & 0 \\ 0 & 0 & -1 & 0 \\ 0 & 0 & 0 & -1 \end{bmatrix}, \tag{4.49}$$

$\vec{p}$ is the momentum operator and *c* and *m* denote the speed of light in vacuum and the rest mass of the electron, respectively. *V* is the external potential given *e.g.* by the electron-nucleus Coulomb interaction. $I_{(4)}$ denotes four-dimensional unit matrix. Solving the one-electron eigenvalue equation:

$$H_D\psi = E\psi, \tag{4.50}$$

we obtain the energy expectation value *E* and the Dirac four-spinor $\psi$. The four-component wave function:

$$\psi = \begin{pmatrix} \psi_1 \\ \psi_2 \\ \psi_3 \\ \psi_4 \end{pmatrix}, \tag{4.51}$$

can be decomposed into two-component parts:

$$\psi = \begin{pmatrix} \psi^L \\ \psi^S \end{pmatrix}, \tag{4.52}$$

where: $\psi^L = \begin{pmatrix} \psi_1 \\ \psi_2 \end{pmatrix}$ and $\psi^S = \begin{pmatrix} \psi_3 \\ \psi_4 \end{pmatrix}$ and $\psi^L$ and $\psi^S$ are called the large and small components, respectively. In general case, for an arbitrary one-electron operator $\hat{O}$, we can calculate its expectation value:

$$O = < \psi \left| \hat{O} \right| \psi >, \tag{4.53}$$

which in the special case of position operator $\hat{O} = \hat{r}$, gives the electron density at the specific position $\vec{\vec{r}}$. The idea of the DKH unitary transformation technique is to block-diagonalize the unperturbed Dirac-Hamiltonian $H_{\mathrm{D}}$ by a suitably chosen unitary transformation:

$$H_{BD} = UH_D U^{\dagger}. \tag{4.54}$$

By applying the same unitary transformation to the unperturbed one-electron wave function $\psi$, we eliminate the small-component $\psi^S$ from the original Dirac-spinor:

$$U\psi = U\begin{pmatrix}\psi^L\\ \psi^S\end{pmatrix} = \begin{pmatrix}\phi^L\\ 0\end{pmatrix} \tag{4.55}$$

This yields the exact two-component DKH wave function $\phi^L$. This idea can be generalized to the many-electron [Wolf 2002]. Since the explicit form of matrix $U$ is not known, it is represented by a sequence of infinite number of unitary matrices $U_m$:

$$U = \ldots U_3 U_2 U_1 U_0 \tag{4.56}$$

In computational implementation, this sequence has to be truncated with respect to predefined order in the external potential $V$. This leads to difereent approximate decoupling schemes which can be classified according to the DKH order of the Hamiltonian. In this work, the calculations in most cases were performed with Douglas-Kroll-Hess second order (DKH2) scalar relativistic Hamiltonian approach implemented into GAUSSIAN *ab initio* package [Frisch 2009]. The calculated electron density $\rho(\vec{r})$ was spherically averaged, using Multiwfn 3.6 code [Lu 2011], in order to obtain the spherically averaged electron density $\rho(r)$. Results of $\rho(r)$ computations for all tungsten ions are presented in Figure 4.9.

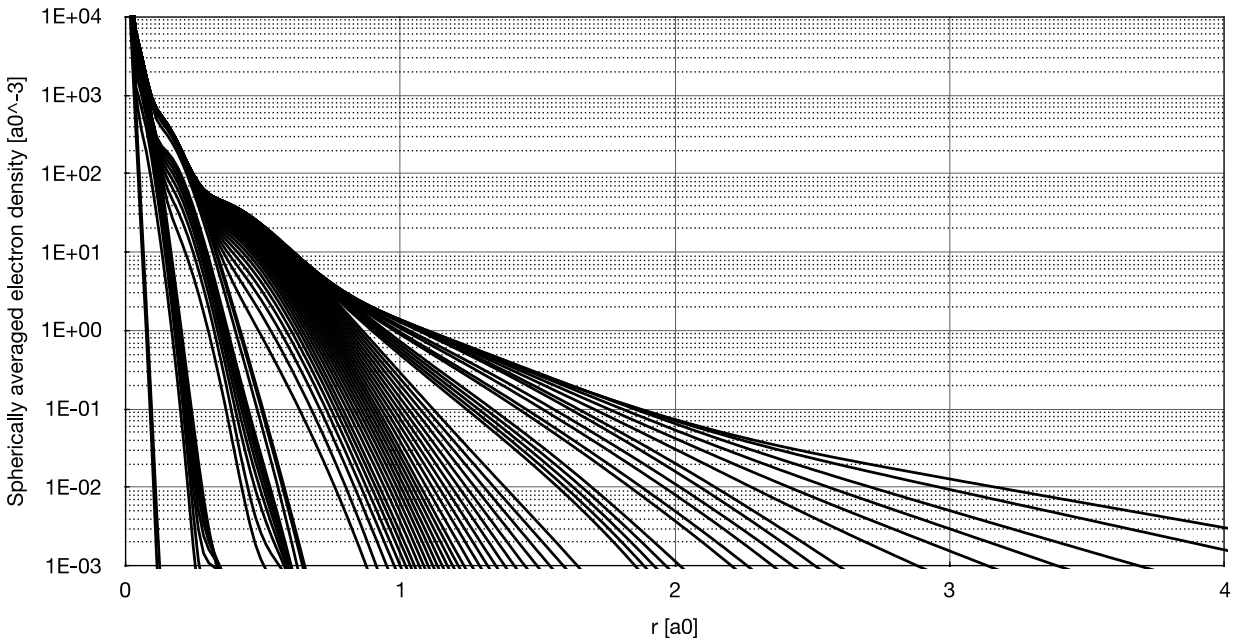


***Figure 4.9.*** *Spherically averaged electron density of tungsten ions.*

### 4.1.4 Comparison between TF – Kirillov and DFT approaches

In order to compare the Thomas-Fermi-Kirillov and DFT approaches described in the previous sections, *Hesslow et al* developed a method to extract an effective ion radius from DFT calculations, expressed as follows:

$$\bar{a}_j = \frac{2}{\alpha} exp\left[\gamma_E - 1 + \frac{2Z_j \hat{I}_{1,j} + N_{e,j}\left(\frac{7}{6} - \hat{I}_{2,j}\right)}{Z_j + Z_{0,j}}\right], \tag{4.57}$$

where the integrals $\hat{I}_{1,j}$ and $\hat{I}_{2,j}$ are detailed in [Hesslow 2018] and are expressed as follows:

$$\hat{I}_{1,j} = \frac{4\pi}{N_{e,j}} \int_0^\infty \rho_{e,j}(r)\, r^2 \ln r \, dr,$$
$$\hat{I}_{2,j} = \frac{(4\pi)^2}{16 N_{e,j}^2} \int_0^\infty \int_0^\infty (s^2 - t^2)\rho_{e,j}\left(\frac{s+t}{2}\right)\rho_{e,j}\left(\frac{s-t}{2}\right)[s^2 \ln s - t^2 \ln t]\, ds\, dt. \tag{4.58}$$

We show here, in Figure 4.10, such a comparison for Argon and Tungsten ions. It is observed that the three methods are globally consistent, although it appears that the Kirillov approximation is much less accurate than the TF method, in particular for low ionization states.

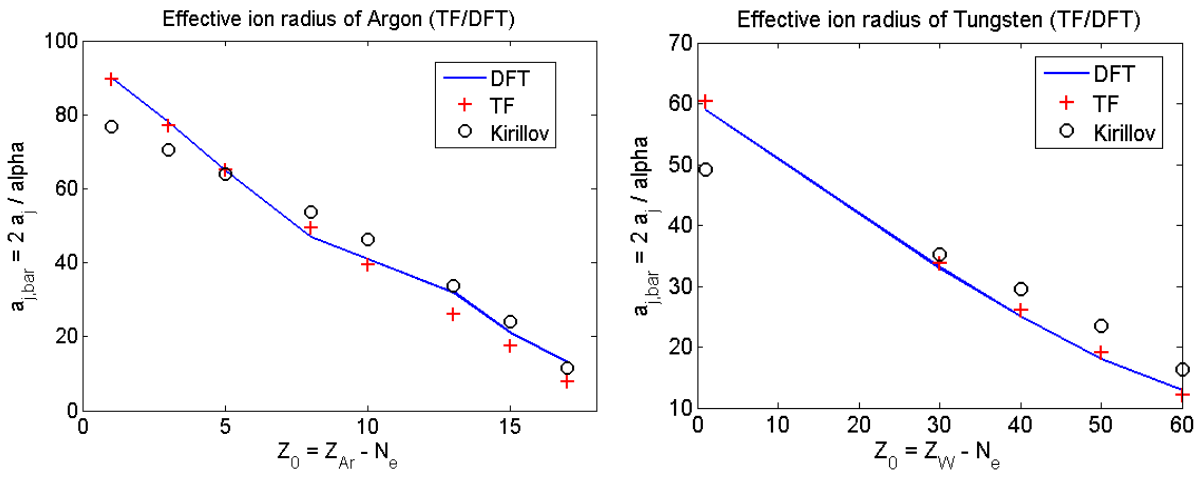


***Figure 4.10.*** *Comparison of the effective ion radius as calculated by the TF, Kirillov and DFT approaches for different ionization stages of (left) Argon, (right) Tungsten.*

## 4.2 Coulomb (elastic) collision cross-section

An application of the atomic form factor calculations performed in the previous sections is to estimate accurately the differential Coulomb ion-electron (elastic) collision cross-section in tokamak plasmas with high-Z impurities, that can be expressed as follows:

$$\frac{d\sigma_{e,j}^{coll}}{d\Omega} = \frac{r_0^2}{4p^4}\left(\frac{\cos^2(\theta/2)\,p^2+1}{\sin^4(\theta/2)}\right)\left|Z_j - F_j(q)\right|^2, \tag{4.59}$$

where $r_0$ denotes the classical electron radius, $\theta$ is the deflection angle and the modified momentum $q = 2p\sin(\theta/2)/\alpha$ with $p = \gamma v/c$. It is clear from Eq. (4.59) that the partial screening effect can impact the collision cross-section through the term $\left|Z_j - F_j(q)\right|^2$ as compared to the complete screening case $\left|Z_j - N_e\right|^2 = {Z_0}^2$. The relative impact of the partial screening effect can be estimated by expressing the electron – ion collision frequency $\nu^{ei}$ as given by [Hesslow 2018]:

$$\nu^{ei} = \nu_{CS}^{ei}\left(1 + \frac{1}{Z_{eff}}\sum_j \frac{n_j}{n_e}\frac{g_j(p)}{\ln\Lambda}\right), \tag{4.60}$$

where $\nu_{CS}^{ei}$ is the collision frequency in the Complete Screening (CS) case, $Z_{eff} = \sum_j n_j {Z_{0,j}}^2/n_e$ is the effective ion charge, $\ln\Lambda$ the Coulomb logarithm and the screening integral $g_j(p)$ is given by:

$$g_j(p) = \int_{1/\Lambda}^{1}\left(\left|Z_j - F_j(q)\right|^2 - Z_{0,j}^2\right)\frac{dx}{x}, \tag{4.61}$$

with $x = sin(\theta/2)$. In the case of one ion species only in the plasma, Eq. (4.60) can be simplified to:

$$\frac{\nu^{ei}}{\nu_{CS}^{ei}} = 1 + \frac{g_j(p)}{Z_0\ln\Lambda}. \tag{4.62}$$

In the TF framework, it was shown that the screening integral can be reduced to the simplified formula:

$$g_j(p) = \frac{2}{3}\left({Z_j}^2 - {Z_0}^2\right)\ln\left[\left(p\bar{a_j}\right)^{3/2}+1\right] - \frac{2}{3}\frac{{N_e}^2\left(p\bar{a_j}\right)^{3/2}}{\left(p\bar{a_j}\right)^{3/2}+1}, \tag{4.63}$$

where $\bar{a_j} = 2a_j/\alpha$. An example is shown on Figure 4.11 for a pure plasma of $Ar^+$ and $W^{40+}$. The Coulomb logarithm is calculated assuming $ln\,\Lambda = 14.9 - 0.5\,ln(n_e\,[10^{20}m^{-3}]) + ln(T_e\,[keV])$. For $Ar^+$, the plasma conditions are $n_e = 10^{20}\,m^{-3}$and $T_e = 10\,eV$ thus $\ln\Lambda = 10.3$, corresponding to a massive gas injection in a post-disruptive tokamak plasma. For $W^{40+}$, the conditions are $n_e = 5\cdot 10^{19}\,m^{-3}$and $T_e = 3\,keV$ thus $ln\,\Lambda = 16.3$, corresponding to regular tokamak plasma core.

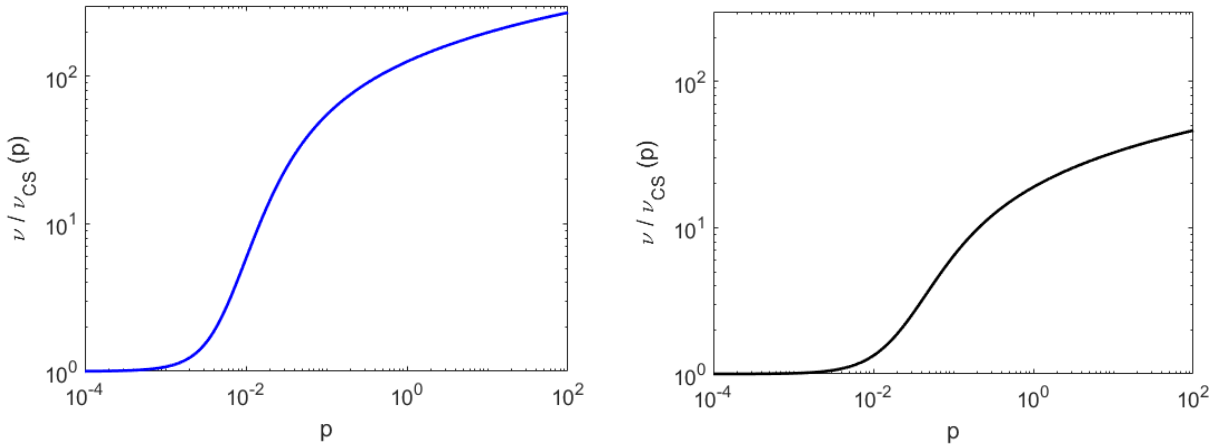


***Figure 4.11.*** *Electron-ion deflection frequency normalized to the Complete Screening (CS) case, for $Ar^+$ (left) and for $W^{40+}$ (right) ions with $\ln \Lambda = 10.3$ and $\ln \Lambda = 16.3$, respectively.*

The electron normalized momentum $p \sim 1$ on the plot corresponds typically to few hundreds *keV*, showing the necessity to include the partial screening effect for high electron energies.

### 4.3 Fast electron bremsstrahlung cross-section

The fast electron-ion Bremsstrahlung differential cross-section is given by the formula (1BS) of [Koch 1959]:

$$\frac{d^5\sigma_{e,j}^{Brem}}{dk d\Omega_k d\Omega_p} = \alpha \left(\frac{r_e}{2\pi}\right)^2 \frac{p}{k p_0 q^4} B(q,\theta,\phi) \left|Z_j - F_j(q)\right|^2, \tag{4.64}$$

with

$q^2 = p^2 + p_0^2 + k^2 - 2p_0 k \cos\theta_0 + 2pk\cos\theta - 2pp_0(\cos\theta\cos\theta_0 + \sin\theta\sin\theta_0\cos\phi)$

where $\vec{k}$ is the wave vector of the emitted photon, $\overrightarrow{p_0}$, $\vec{p}$ are the initial and final electron momentum, $\theta_0$, $\theta$ the associated angles with respect to $\vec{k}$, and $\varphi$ is the angle between the $(\overrightarrow{p_0}, \vec{k})$ plane and the $(\vec{p}, \vec{k})$ plane as depicted on Figure 4.12. Additionnaly, the term $B(q,\theta,\phi)$ is decomposed as follows:

$$B(q,\theta,\phi) = \sum_{k=1}^{4} B_k, \tag{4.65}$$

with:

$$\begin{aligned}
B_1 &= \frac{p^2 \sin^2\theta}{(E - p\cos\theta)^2}(4E_0^2 - q^2), \\
B_2 &= \frac{p_0^2 \sin^2\theta_0}{(E_0 - p_0\cos\theta_0)^2}(4E^2 - q^2), \\
B_3 &= \frac{2pp_0 \sin\theta \sin\theta_0 \cos\phi}{(E - p\cos\theta)(E_0 - p_0\cos\theta_0)}(4EE_0 - q^2), \\
B_4 &= \frac{2k^2(p^2\sin^2\theta + p_0^2\sin^2\theta_0 - 2pp_0\sin\theta\sin\theta_0\cos\phi)}{(E - p\cos\theta)(E_0 - p_0\cos\theta_0)}.
\end{aligned} \tag{4.66}$$

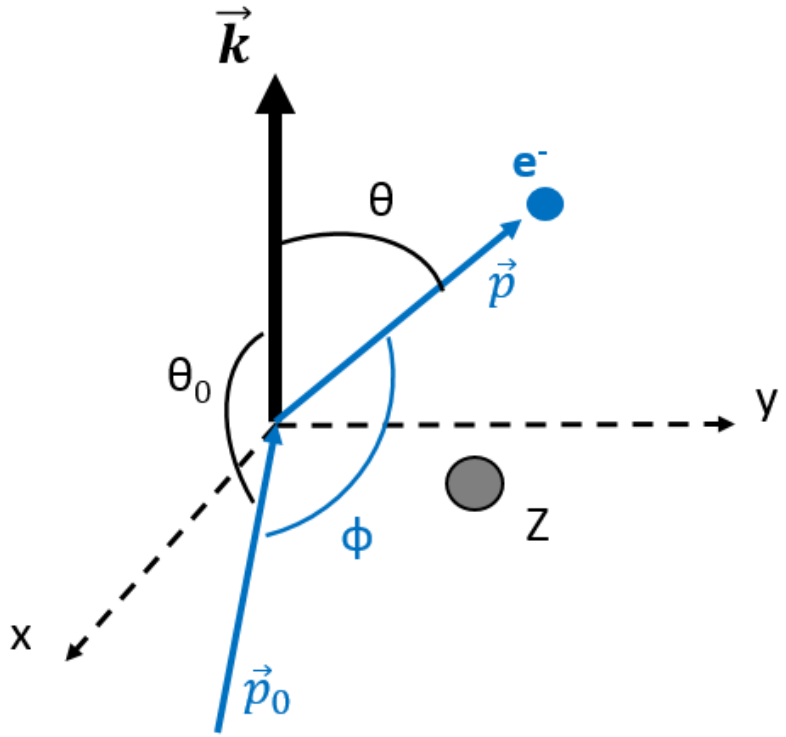


***Figure 4.12.*** *Fast electron ion Bremsstrahlung, where $\vec{k}$ is the wave vector of the emitted photon, $\vec{p_0}$, $\vec{p}$ are the initial and final electron momentum, $\theta_0$, $\theta$ the associated angles with respect to $\vec{k}$, and $\varphi$ is the angle between the ($\vec{p_0}$, $\vec{k}$) plane and the ($\vec{p}$, $\vec{k}$) plane.*

The integration over over $\phi$ and $\theta$ angles leads to:

$$\frac{d^3\sigma_{e,j}^{Brem}}{dkd\Omega_k} = \int_0^{\pi} \sin\theta \int_0^{2\pi} \frac{d^5\sigma_{e,j}^{Brem}}{dkd\Omega_k d\Omega_p} d\phi \, d\theta. \tag{4.67}$$

We can obtain for the integration over $\phi$:

$$\int_0^{2\pi} \frac{d^5\sigma_{e,j}^{Brem}}{dkd\Omega_k d\Omega_p} d\phi = \alpha \left(\frac{r_e}{2\pi}\right)^2 Z_s^2 \frac{p}{kp_0} \sum_{k=1}^{4} \int_0^{2\pi} \left(1 - \frac{F_j(q)}{Z_s}\right)^2 B_k \frac{d\phi}{q^4}, \tag{4.68}$$

leading to a sum of integrals $J_k$, $k \in [1;4]$:

$$\int_0^{2\pi} \frac{d^5\sigma_{e,j}^{Brem}}{dkd\Omega_k d\Omega_p} d\phi = Z_s^2 \frac{p}{kp_0} \sum_{k=1}^{4} a_k J_k, \tag{4.69}$$

where $a_k$ are coefficients that can be easily determined from the previous equations and $J_k$ are expressed as:

$$J_1 = \int_0^{2\pi} \left(1 - \frac{F_j(q)}{Z_j}\right)^2 \frac{d\phi}{q^4}, \tag{4.70}$$

$$J_2 = \int_0^{2\pi} \left(1 - \frac{F_j(q)}{Z_j}\right)^2 \frac{d\phi}{q^2},$$

$$J_3 = \int_0^{2\pi} \left(1 - \frac{F_j(q)}{Z_j}\right)^2 \cos\phi \frac{d\phi}{q^4},$$

$$J_4 = \int_0^{2\pi} \left(1 - \frac{F_j(q)}{Z_j}\right)^2 \cos\phi \frac{d\phi}{q^2}.$$

Using the fact that the atomic form factor can be expressed, from the Tseng-Pratt model, as:

$$F_j(q) = \frac{N_{e,j}}{1 + \left(qa_j\right)^2}, \tag{4.71}$$

where $N_{e,j} = Z_j - Z_{0,j}$, the expression in Eq. (4.70) can be reformulated as:

$$\left(1 - \frac{F_j(q)}{Z_j}\right)^2 = \left(1 - \frac{1 - q_j}{1 + \left(qa_j\right)^2}\right)^2 = 1 - \frac{2\left(1 - q_j\right)}{1 + \left(qa_j\right)^2} + \frac{\left(1 - q_j\right)^2}{\left(1 + \left(qa_j\right)^2\right)^2}, \tag{4.72}$$

where $q_j = Z_{0,j}/Z_j$ is the ionization degree. Therefore, the four integrals can be split into twelve integrals: $J_m = J_{m,1} + J_{m,2} + J_{m,3}$ with $m \in \{1,4\}$.

It is possible to write:

$$q^2 = a\cos\phi + b, \tag{4.73}$$

with $b = p^2 + p_0^2 + k^2 - 2p_0 k\cos\theta - 2pp_0\cos\theta\cos\theta_0 \geq 0$,

and $a = -2pp_0\sin\theta\sin\theta_0\cos\phi < 0$,

with the condition: $-b/a > 1$.

Therefore, the $J_k$ integrals can take the general form:

$$J_k = \int_0^{2\pi} \left(1 - \frac{1 - q_j}{1 + (a\cos\phi + b)a_j^2}\right)^2 (\cos\phi)^p \frac{d\phi}{(a\cos\phi + b)^n}. \tag{4.74}$$

Therefore, the expansion using the Tseng-Pratt model implies that:

$$J_k = \int_0^{2\pi} \frac{(cos\,\phi)^p}{(a\,cos\,\phi + b)^n} d\phi - 2\left(1 - q_j\right) \int_0^{2\pi} \frac{(cos\,\phi)^p}{(a\,cos\,\phi + b)^n \left(1 + (a\,cos\,\phi + b) a_j^2\right)} d\phi + \left(1 - q_j\right)^2 \int_0^{2\pi} \frac{(cos\,\phi)^p}{(a\,cos\,\phi + b)^n \left(1 + (a\,cos\,\phi + b) a_j^2\right)^2} d\phi.$$

This can be rewritten as:

$$J_k = \hat{J}_{k,1}^{TP} - 2\left(1 - q_j\right) \hat{J}_{k,2}^{TP} + \left(1 - q_j\right)^2 \hat{J}_{k,3}^{TP}, \tag{4.75}$$

leading to the twelve integrals $\hat{J}_{k,l}^{TP}$, $k \in \{1,2,3,4\}$; $l \in \{1,2,3\}$:

$$\hat{J}_{k,l}^{TP} = \int_0^{2\pi} \frac{(cos\,\phi)^p d\phi}{(a\,cos\,\phi + b)^n (1 + (a\,cos\,\phi + b) c^{TP})^m}, \tag{4.76}$$

with the following values $p \in \{0,1\}$; $n \in \{1,2\}$; $m \in \{0,1,2\}$. For the most simple cases $m = 0$, due to the fact that $cos(\phi + \pi) = -cos\,\phi$, we have:

$$\hat{J}_{k,l}^{TP} = \int_0^{2\pi} \frac{(cos\,\phi)^p}{(a\,cos\,\phi + b)^n} d\phi = 0.$$

The eight remaining integrals $\hat{J}_{k,l}^{TP}$ are all solved analytically, see the details of the calculations in the Appendix, and compared to the numerical integration for validation purposes.

# 5. Selected experimental data

## 5.1 First SXR tomographic tests on WEST

In 2019, the new GEM detector was still under installation on the WEST vertical port. Therefore, only the horizontal former SXR camera was operational. This means that the information on line-integrated data along the vertical direction was missing when performing tomographic inversion. In order to compensate this temporary loss of information, a strong additional constraint was imposed on the reconstruction by using preferential smoothing along the magnetic flux surfaces. Preliminary results are shown below:

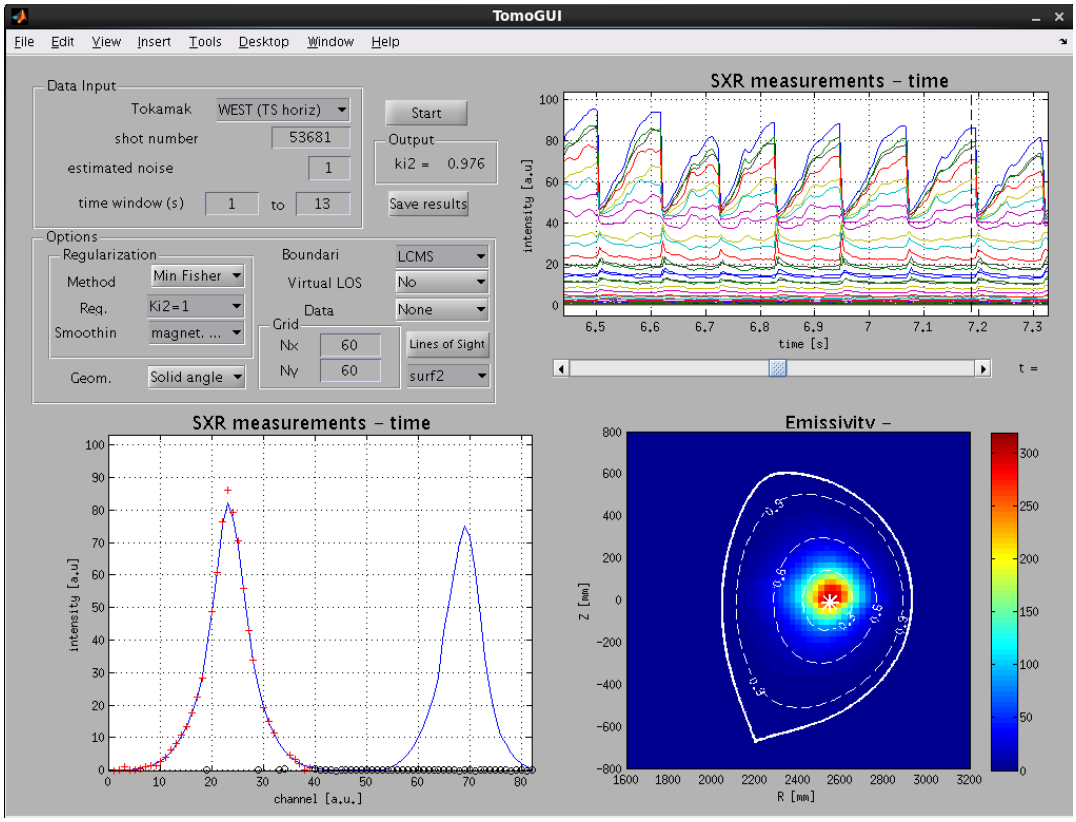


***Figure 5.1.*** *Attempt of SXR experimental tomography on WEST discharge #53681 just before a sawtooth crash, using the former horizontal camera only and with preferential smoothing along the flux surfaces.*

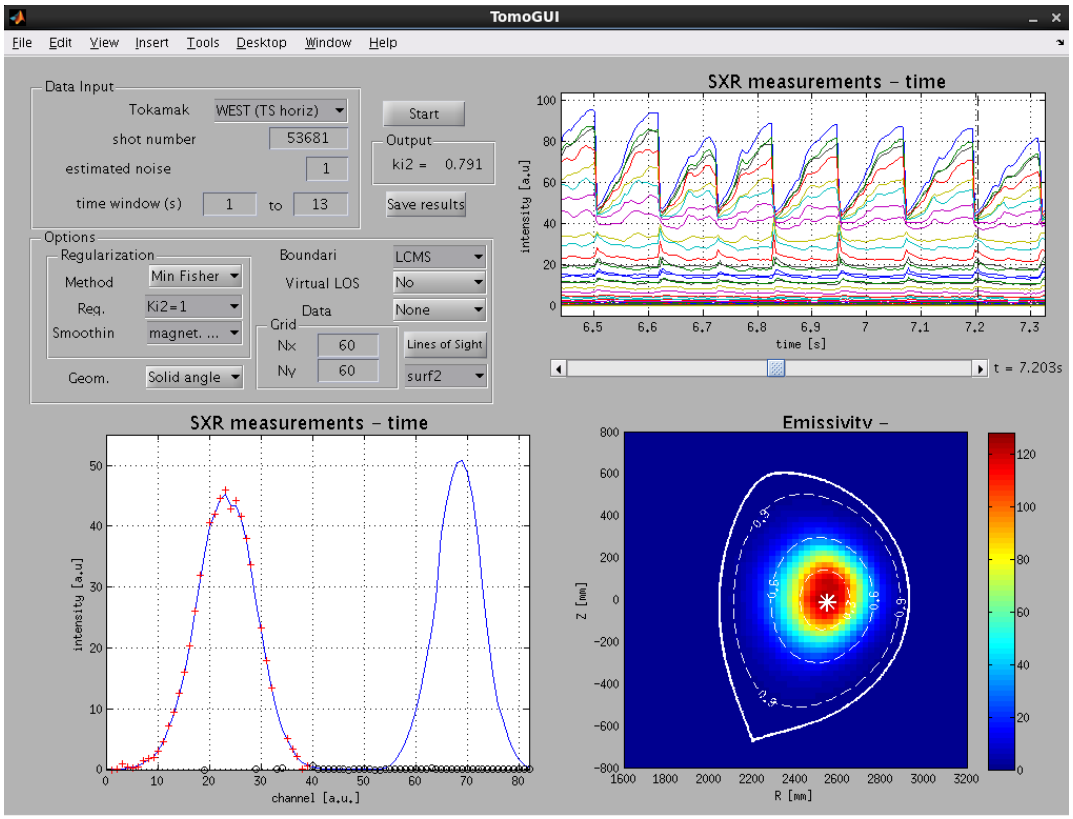


***Figure 5.2.*** *Attempt of SXR experimental tomography on WEST discharge #53681 just after a sawtooth crash, using the former horizontal camera only and with preferential smoothing along the flux surfaces.*

It can be seen that the SXR profile is significantly peaked in the plasma core just before the sawtooth crash. This can be an evidence of the presence of impurities (tungsten, copper, …). As expected, the SXR profile is broader after the sawtooth crash due to electron density flattening and redistribution of impurities in the plasma core. This developed tool will be useful in the next steps of the project since it reconstructs the SXR profile from the horizontal camera only and will allow to predict, thanks to a GEM synthetic diagnostic, what should be the SXR measurements of the GEM vertical camera. This will be very valuable for validation and cross-checking of the new GEM diagnostic.

### 5.1 Identification of valuable Tore Supra and WEST plasma discharges

Some valuable Tore Supra and WEST plasma discharges have been identified for the above mentioned studies in 2019-2020. This database will continue to be developed in 2020-2022.

***Table 5.1.*** *Tore Supra / WEST discharges under investigation*

| Discharge | SXR | HXR | LHCD | Impurities | Comments |
|---|---|---|---|---|---|
| 46564 | Yes | No | Yes | W LBO | Very valuable but no HXR data |
| 36420 | Yes | | No | | SXR modulation → plasma position shift to the left |
| 36421 | Yes | | No | | SXR modulation |
| 36423 | Yes | | | No | SXR signal poor |
| 36424 | Yes | Yes | Yes | No | |
| 36425 | Yes | Yes | Yes | No | Artefact in SXR tomo |
| 36426 | Yes | Yes | Yes | Injection at t=8.4s? | LBO ? MHD (sawteeth) |
| 36427 | Yes | Yes | Yes | No | |
| 36428 | Yes | Yes | Yes | No | |
| 41864 | | | | No | |
| 48174 | | | | t = 5s? | |
| 36782 | | | | Injection? | |
| 31527 | | | | | [Nillson et al. 2013] |
| 45155 | | | | | [Decker et al. 2014] |
| 45525 | | | | | [Nillson et al. 2013] |
| 53681 | Yes | | | | Sawteeth oscillations |
| 54952 | | | | | [Y. Peysson et al. 2020] |
| 55539 | | | | | [Y. Peysson et al. 2019] |

## 6. Conclusion and perspectives

In this report, the preparatory work performed during the first year of the HARMONIA collaboration project between IFJ PAN and IRFM (CEA) has been introduced and described in details. The state of the art on LH current drive and heavy impurities is made and the research equipments (WEST tokamak, X-ray diagnostics) and methods (reconstruction methods, chain of numerical codes ALOHA-C3PO-LUKE-R5X2) necessary for the project are described. Some models are introduced to include the partial screening effect in the fast electron dynamics in tokamak plasmas with high-Z impurities, namely the Thomas-Fermi model, Tseng-Pratt model and the GAUSSIAN calculations based on the Density Functional Theory (DFT). The simplified models allow the derivation of analytical solutions for the

atomic form factor and for the Bremsstrahlung cross-sections, while the accuracy of numerical DFT calculations is necessary to benchmark the simplified models. This preparatory work is necessary to include the partial screening effect in the set of numerical codes available at IRFM. A set of experimental data from Tore Supra and WEST plasma discharges have been selected. The key diagnostics will be the SXR and HXR tomography systems to monitor the impurity and fast electron distributions, respectively, during the selected plasma discharges. They will allow investigating the impact of heavy impurities on LH current drive efficiency and fast electron Bremsstrahlung intensity and determining quantitatively the contribution of the partial screening effect.

## Acknowledgements

This research was supported in part by the PL-Grid Infrastructure and by the HARMONIA Grant nr 2018/30/M/ST2/00799.

## Bibliography

[ADAS] The Atomic Data and Analysis Structure (ADAS) project: http://open.adas.ac.uk

[Angioni 2015] C. Angioni et al, The impact of poloidal asymmetries on tungsten transport in the core of JET H-mode plasmas, Physics of Plasmas 22 (2015) 055902.

[Anton 1996] M Anton et al, X-ray tomography on the TCV tokamak, 1996 Plasma Phys. Control. Fusion 38 1849.

[Artaud 2018] F. Artaud et al, Metis: a fast integrated tokamak modelling tool for scenario design, Nuclear Fusion 58 (2018) 105001.

[Becke 1993] A. Becke, A new mixing of Hartree–Fock and local density-functional theories, The Journal of Chemical Physics, 1993, Vol. 98, p. 1372.

[Belo 2005] J.H. Belo et al, ITER-like PAM launcher for Tore Supra's LHCD system, Fusion Engineering and Design 74 (2005) 283–288.

[Bernabai 1997] S. Bernabei, A. Cardinali, G. Giruzzi, G. T. Hoang, D. Ignat, R. Kaita, M. Okabayashi, F. Paoletti, and S. Von Goeler, Phys. Plasmas 4, 125 (1997).

[Bielecki 2018a] J. Bielecki, A genetic algorithm-based method of neutron emissivity tomographic inversion for tokamak plasma, Fusion Engineering and Design 127 (2018) 160–167.

[Bielecki 2018b] J. Bielecki, Metropolis–Hastings Monte Carlo Method for Neutron Emissivity Tomographic Inversion in Tokamak Plasma, Journal of Fusion Energy 2018

[Bilato 2017] R. Bilato, O. Maj and C. Angioni, Modelling the influence of temperature anisotropies on poloidal asymmetries of density in the core of rotating plasmas, Nuclear Fusion 54 (2014) 072003.

[Challis 1989] Challis, C. D., et al., Non-inductively driven currents in JET, Nuclear fusion 29.4 (1989): 563.

[Colo 2018] G. Colo, Heavy nuclei: Introduction to density functional theory and variations on the theme, The European Physical Journal Plus, 2018, Vol. 133, p. 553.

[Craciunescu 2008] T. Craciunescu, G. Bonheure, V. Kiptily, A. Murari, S. Soare, I. Tiseanu, V. Zoita, The maximum likelihood reconstruction method for JET neutron tomography, Nucl. Instrum. Meth. A 595 (2008) 623.

[Craciunescu 2009] T. Craciunescu, G. Bonheure, V. Kiptily, A. Murari, I. Tiseanu, V. Zoita, A Comparison of Four Reconstruction Methods for JET Neutron and Gamma Tomography, Nucl. Instrum. Methods A 595 (2009) 374.

[Csavinszky 1969] P. Csavinszky, Approximate Analytical Solutions of the Thomas-Fermi Equation for Positive Ions, J. Chem. Phys. 50, 1176 (1969).

[Douglas 1974] M. Douglas, N. Kroll, Quantum electrodynamical corrections to the fine structure of helium, Annals of Physics, 1974, Vol. 82, pp. 89-155.

[Fermi 1928] E. Fermi, Eine statistische Methode zur Bestimmung einiger Eigenschaften des Atoms und ihre Anwendung auf die Theorie des periodischen Systems der Elemente, Zeitschrift für Physik, 1928, Vol. 48.

[Fidone 1984] I. Fidone, G. Giruzzi, G. Granata, and R. L. Meyer, Phys. Fluids 27, 2468 (1984).

[Fisch 1987] N. Fisch, Rev. Mod. Phys. 59 (1987) 175.

[Garbet 1994] X. Garbet et al., Proc. of the 15th Conf. on Plasma Phys. and Control. Nuclear Fusion, Seville, 1 (1994) 105.

[Ghendrih 2015] P. Ghendrih et al, The WEST Research Plan, IFRM, CEA Cadarache, 2015.

[Giruzzi 1989] G. Giruzzi, I. Fidone, and R. L. Meyer, Nucl. Fusion 29, 1381 (1989).

[Granetz 1988] R.S. Granetz and P. Smeulders, X-ray tomography on JET, 1988 Nucl. Fusion 28 457.

[Gronowski 2017] M. Gronowski, TD-DFT benchmark: Excited states of atoms and atomic ions, Computational and Theoretical Chemistry, 2017, Vol. 1108, pp. 50-56.

[Guosheng 2007] X. Guosheng, W. Baonian, An Analytical Method for the Abel Inversion of Asymmetrical Gaussian Profiles, Plasma Science and Technology, Vol.9, No.1, Feb. 2007.

[Hasnip 2011] P. Hasnip K. Refson M. Probert, J. Yates, S. Clark, C. Pickard Density functional theory in the solid, Philosophical Transactions of The Royal Society A Mathematical Physical and Engineering Sciences, 2011, Vol. 372, p. 20130270.

[Hess 1985] B. Hess, Applicability of the no-pair equation with free-particle projection operators to atomic and molecular structure calculations, Physical Review A. 1985, Vol. 32, pp. 756-763.

[Hesslow 2017] L. Hesslow, O. Embréus, A. Stahl, T. C. DuBois, G. Papp, S. L. Newton, and T. Fülöp, Effect of Partially Screened Nuclei on Fast-Electron Dynamics, Phys. Rev. Lett. 118 (2017) 255001.

[Hesslow 2018] L. Hesslow, O. Embreus, M. Hoppe, T. C. DuBois, G. Papp, M. Rahm and T. Fulop. Generalized collision operator for fast electrons interacting with partially ionized impurities. J. Plasma Phys. 84 (2018) 905840605.

[Hillairet 2010] J. Hillairet et al, ALOHA: an Advanced LOwer Hybrid Antenna coupling code, Nucl. Fusion 50 (2010) 125010.

[Hohenberg 1964]. P. Hohenberg W Kohn Inhomogeneous electron gas, Physical Review, 1964, Vol. 136, pp. B864–B871.

[Imrisek 2016] M. Imrisek et al, Optimization of soft X-ray tomography on the COMPASS tokamak, Nukleonika 61 (2016) 403-408.

[Ingesson 1998] L.C. Ingesson et al, Soft X ray tomography during ELMs and impurity injection in JET, 1998 Nucl. Fusion 38 1675.

[Jardin 2016a] A. Jardin et al, Tomographic capabilities of the new GEM based SXR diagnostic of WEST, 2016 JINST 11 C07006.

[Jardin 2016b] A. Jardin, D. Mazon and J. Bielecki, Comparison of two regularization methods for soft x-ray tomography at Tore Supra, Physica Scripta 91 (2016) 044007.

[Jardin 2017] A. Jardin et al, On a Gas Electron Multiplier based synthetic diagnostic for soft x-ray tomography on WEST with focus on impurity transport studies, 2017 JINST 12 C08013.

[Jardin 2018] A. Jardin, J. Bielecki, D. Mazon, J. Dankowski, K. Król, Y. Peysson and M. Scholz, Neural networks for fast soft X-ray tomographic inversions in tokamaks, in proceedings of the 45th EPS Conference on Plasma Physics, P4.1013.

[Johnston 2017] H. Johnston et al., WEST tokamak fires up first plasma, Phys. World 30 (2017) 11.

[Kim 1974] Y. Kim, R.Gordon, Study of the electron gas approximation, Journal of Chemical Physics, 1974, Vol. 60, pp. 1842 - 1850.

[Kirillov 1975] V. D. Kirillov, B.A. Trubnikov, and S.A Trushin. Role of impurities in anomalous plasma resistance. Fizika Plazmy, 1 :218 – 237, Mar - Apr 1975.

[Koch 1959] H. W. Koch and J. W. Motz, Bremsstrahlung cross-section formulas and related data, Rev. Mod. Phys., 31(4) :920, 1959.

[Kohn 1965] W. Kohn J. Sham, Self-Consistent Equations Including Exchange and Correlation Effects, Physical Review, 1965, Vol. 1133, p. A1133.

[Lamoureux 1997] M. Lamoureux and N. Avdonina. Bremsstrahlung in hot plasmas with partially ionized atoms. PHYSICAL REVIEW E, 55(1) :912–926, 1997.

[Li 2001] X. Li Z. Cai, M. Sevilla, Investigation of Proton Transfer within DNA Base Pair Anion and Cation Radicals by Density Functional Theory (DFT), The Journal of Physical Chemistry B, 2001, Vol. 105, pp. 10115-10123.

[Lipiec 2014] E. Lipiec R. Sekine J. Bielecki, W. Kwiatek, B. Wood, Molecular Characterization of DNA Double Strand Breaks with Tip-Enhanced Raman Scattering , Angewandte Chemie International Edition, 2014, Vol. 53, pp. 169-172.

[Louche 1998] Louche, F. (1998). A solver for the non-linear Fokker-Planck equation. In Rogister, A. (Ed.). Fusion theory Proceedings, (p. 319). Germany.

[Lu 2011] T. Lu F. Chen Multiwfn: A multifunctional wavefunction analyzer, Journal of Computational Chemistry, 2011 Vol. 33.

[Lundqvist 1983] S. Lundqvist, N. H. March, Theory of the inhomogeneous electron gas, Springer Book (1983) ISBN 978-1-4899-0415-7.

[Maj 2012] O. Maj, E. Poli, E. Westerhof, Journal of Physics: Conference Series 401 (2012). 012013.

[Mazon 2012] D. Mazon, D. Vezinet et al., Soft x-ray tomography for real-time applications: present status at Tore Supra and possible future developments, Review of Scientific Instruments, vol. 83, no.6 (2012).

[Mazon 2013] D. Mazon et al, Soft X-ray imaging techniques on Tore Supra: Present status and possible future developments, Nuclear Instruments and Methods in Physics Research A 720 (2013) 78–82.

[Mazon 2015] D. Mazon et al, Design of soft-X-ray tomographic system in WEST using GEM detectors, Fusion Engineering and Design 96–97 (2015) 856-860.

[Mazon 2017] D. Mazon et al, SXR measurement and W transport survey using GEM tomographic system on WEST, 2017 JINST 12 C11034.

[Mlynar 2012] J. Mlynar, M. Imrisek, V. Weinzettl, M. Odstrcil, J. Havlicek, F. Janky, B. Alper, A. Murari, and JETEFDA Contributors, Introducing minimum Fisher regularisation tomography to AXUV and soft x-ray diagnostic systems of the COMPASS tokamak, Review of Scientific Instruments 83, 10E531 (2012).

[Nilsson 2013] E. Nilsson et al, Comparative modelling of lower hybridcurrent drive with two launcher designsin the Tore Supra tokamak, Nucl. Fusion 53(2013) 083018.

[Odstrcil 2016] T. Odstrcil et al, Optimized tomography methods for plasma emissivity reconstruction at the ASDEX Upgrade tokamak, Review of Scientific Instruments 87, 123505 (2016)

[Oikawa 2000] Oikawa, T., et al. , Heating and non-inductive current drive by negative ion based NBI in JT-60U, Nuclear Fusion 40.3Y (2000) 435.

[Parr 1995] R. G. Parr W. Yang, Density-Functional Theory of the Electronic Structure of Molecules, Annual Review of Physical Chemistry, 1995, Vol. 46, pp. 701-728.

[Perdew 1996] J. Perdew, M. Ernzerhof and K. Burke, Rationale for mixing exact exchange with density functional approximations, The Journal of Chemical Physics, 1996, Vol. 105, pp. 9982–9985.

[Peysson 1999] Y. Peysson, in Radio Frequency Power in Plasmas (American Institute of Physics, Melville, NY, 1999), 183.

[Peysson 2000] Peysson, Y., and Tore Supra Team ,Progress towards high-power lower hybrid current drive in Tore Supra, Plasma Physics and Controlled Fusion 42.12B (2000) B87.

[Peysson 2001] Y. Peysson S. Coda, F. Imbeaux, Hard X-ray CdTe tomography of tokamak fusion plasmas, Nuclear Instruments and Methods in Physics Research A 458 (2001) 269-274.

[Peysson 2008] Y. Peysson and J. Decker. Fast electron bremsstrahlung in axisymmetric magnetic configuration. Phys. Plasmas, 15(9) :092509, 2008.

[Peysson 2012] Y. Peysson, J. Decker and L. Morini, A versatile ray-tracing code for studying RF wave propagation in toroidal magnetized plasmas, Plasma Phys. Control. Fusion 54 (2012) 045003

[Peysson 2014] Y. Peysson and J. Decker. Numerical simulations of the radio-frequency driven toroidal current in tokamaks. Fusion Science and Technology, 65:22–42, 2014.

[Peysson 2019] Y. Peysson, K. Krol, A. Jardin, Screening effect of partially ionized high-Z impurities in relativistic linearized bounce-averaged electron Fokker-Planck calculations for RF current drive and runaway electron dynamics, Internal notes, October 2019.

[Pitts 2019] R. A. Pitts et al, Physics Basis of the first ITER divertor, Nuclear Materials and Energy 20 (2019) 100696.

[Pratt 1972] R. H. Pratt and H. K. Tseng. Behavior of electron wave functions near the atomic nucleus and normalization screening theory in the atomic photoeffect. Phys. rev. A, 5(3) :1063, 1972.

[Puetterich 2010] T. Puetterich et al, Calculation and experimental test of the cooling factor of tungsten, nuclear fusion 50 (2010) 025012.

[Raman 2001] Raman, Roger, et al., Non-inductive current generation in NSTX using coaxial helicity injection, Nuclear fusion 41.8 (2001): 1081.

[Roos 2005] B. Roos, R. Lindh, P. Malmqvist, V. Veryazov, P. Widmark, New Relativistic ANO Basis Sets for Transition Metal Atoms, The Journal of Physical Chemistry A., 2005, pp. 6575-6579.

[Shoucri 1994] M. Shoucri and I. Shkarofsky, A Fast 2D Fokker-Planck Solver With Synergetic Effects, Comput. Phys. Commun. 82: 287 (1994).

[Tanaka 1991] Tanaka, H., et al. Non-inductive current drive using second harmonic electron cyclotron waves on the WT-3 tokamak, Nuclear fusion 31.9 (1991) 1673.

[Turck 1989] B. Turck, Tore Supra: a tokamak with superconducting toroidal field coils-status report after the first plasmas Magnetics, IEEE Transactions 25 (1989) 1473 – 1480.

[Wesson 1997] J.A. Wesson, Poloidal distribution of impurities in a rotating tokamak plasma, Nuclear Fusion 37 (1997) 577.

[Wolf 2002] A. Wolf M. Reiher, B. Hess P. Schwerdtfeger (Ed.) Relativistic Quantum Chemistry – Part I. Fundamentals, Theoretical and Computational Chemistry, Amsterdam : Elsevier, 2002, p. 622.

[Zhang 2017] L. Zhang et al, Suppression of tungsten accumulation during ELMy H-mode by lower hybrid wave heating in the EAST tokamak, Nuclear Materials and Energy 12 (2017) 774–778.

# **Annex.** Screening integrals (Tseng-Pratt atomic model)

In the following Appendix, the solutions of the eight integrals: $\hat{J}^{TP}_{1,2}$, $\hat{J}^{TP}_{1,3}$, $\hat{J}^{TP}_{2,2}$, $\hat{J}^{TP}_{2,3}$, $\hat{J}^{TP}_{3,1}$, $\hat{J}^{TP}_{3,2}$, $\hat{J}^{TP}_{4,2}$,$\hat{J}^{TP}_{4,3}$ are detailed. These integrals take the following general form:

$$\hat{J}^{TP}_{k,l} = \int_0^{2\pi} \frac{(cos\phi)^p \, d\phi}{(acos\phi + b)^n \, (1 + (acos\phi + b)c^{TP})^m} \tag{1}$$

where $p,n,m,k,l$ may have the following values $p = 0,1$; $n = 1,2$; $m = 1,2$; $k = 1,2,3,4$; $l = 2,3$. In this whole Appendix $a$ and $b$ satisfy the following conditions

$$\begin{cases} a < 0 \\ b > 0 \\ |b| > |a| \end{cases} \tag{2}$$

The procedure of solving these integrals depends on the value of p. The two cases p = 0 and p = 1 will be considered separately.

## Case p = 0

After introducing $\delta$

$$\delta = \frac{b}{a} < -1 \tag{3}$$

the integral takes the following form

$$\hat{J^{TP}}_{k,l} = \int_0^{2\pi} \frac{d\phi}{(cos\phi + \delta)^n \, (1 + (acos\phi + \delta) \, ac^{TP})^m} \frac{1}{a^n}$$

In order to solve the integral one can use the tangent half-angle substitution

$$x = \tan\frac{\phi}{2} \tag{4}$$

$$dx = \frac{1}{2}\left(1 + x^2\right) d\phi \tag{5}$$

$$\cos\phi = \frac{1 - \tan^2\frac{\phi}{2}}{1 + \tan^2\frac{\phi}{2}} \tag{6}$$

After changing variables, the integral takes the form

$$\begin{aligned} f_{k,l}^{TP} &= \int_{-\infty}^{\infty} \frac{\frac{2}{1+x^2}dx}{\left(\frac{1-x^2}{1+x^2}+\delta\right)^n \left(1+\left(\frac{1-x^2}{1+x^2}+\delta\right)ac^{TP}\right)^m} \frac{1}{a^n} \\ &= \int_{-\infty}^{\infty} \frac{\left(1+x^2\right)^{m+n-1}}{\left(\delta+1+x^2(\delta-1)\right)^n \left(1+x^2+(\delta+1+x^2(\delta-1))ac^{TP}\right)^m} \frac{2}{a^n} \end{aligned} \tag{7}$$

After the factors have been ordered in relation to the powers of x, the integral takes form

$$J_{k,l}^{\hat{TP}} = \int_{-\infty}^{\infty} \frac{\left(1+x^2\right)^{m+n-1}}{\left(\delta+1+x^2(\delta-1)\right)^n \left((1+ac^{TP}(\delta-1))x^2+(1+ac^{TP}(\delta+1))\right)^m} \frac{2}{a^n} \tag{8}$$

To simplify one can introduce new constants

$$A_0 = \delta - 1 \tag{9}$$

$$B_0 = \delta + 1 \tag{10}$$

$$C_0 = 1 + ac^{TP}(\delta - 1) \tag{11}$$

$$D_0 = 1 + ac^{TP}(\delta + 1) \tag{12}$$

Then the integral takes the form

$$J^{\hat{TP}}{}_{k,l} = \frac{2}{a^n} \int_{-\infty}^{\infty} \frac{\left(1+x^2\right)^{m+n-1} dx}{\left(A_0x^2+B_0\right)^n \left(C_0x^2+D_0\right)^m} \tag{13}$$

It is possible once again to simplify and reduce the number of constants by introducing $A$ and $B$ constants

$$A = \frac{B_0}{A_0} = \frac{\delta+1}{\delta-1} > 0 \tag{14}$$

$$B = \frac{D_0}{C_0} = \frac{1+ac^{TP}(\delta+1)}{1+ac^{TP}(\delta-1)} > 0 \tag{15}$$

Since the integrated function is symmetrical, the integral can be written with the following limits

$$J_{k,l}^{\hat{TP}} = \frac{4}{a^n} \frac{1}{A_0^n C_0^m} \int_0^{\infty} \frac{\left(1+x^2\right)^{m+n-1}}{\left(x^2+A\right)^n \left(x^2+B\right)^m} dx \tag{16}$$

One can solve the above integral by using the partial fraction decomposition method

$$\begin{aligned} \frac{\left(1+x^2\right)^{m+n-1}}{\left(x^2+A\right)^n \left(x^2+B\right)^m} &= \sum_{j=1}^{n} \frac{T_j}{\left(x^2+A\right)^j} + \sum_{j=1}^{m} \frac{T_{j+n}}{\left(x^2+B\right)^j} \\ &= \frac{\sum_{j=1}^{n} T_j \left(x^2+A\right)^{n-j} \left(x^2+B\right)^m}{\left(x^2+A\right)^n \left(x^2+B\right)^m} \\ &+ \frac{\sum_{j=1}^{m} T_{j+n} \left(x^2+A\right)^n \left(x^2+B\right)^{m-j}}{\left(x^2+A\right)^n \left(x^2+B\right)^m} \end{aligned} \tag{17}$$

where $T_j \in [1; m+n]$ are coefficients to calculate.

$$\sum_{j=0}^{m+n-1} \left( \begin{array}{c} m+n-1 \\ j \end{array} \right) x^{2j} \equiv \sum_{j=1}^{n} T_j \left(x^2+A\right)^{n-j} \left(x^2+B\right)^m + \sum_{j=1}^{m} T_{j+n} \left(x^2+A\right)^n \left(x^2+B\right)^{m-j} \tag{18}$$

Now, based on the above equation it is possible to write a system of m+n equations with m+n unknowns. Solving this system allows obtaining $T_j \in [1; m+n]$.

$$J^{\hat{TP}}{}_{k,l} = \frac{4}{a^n} \frac{1}{A_0^n C_0^m} \left( \sum_{j=1}^{n} T_j \int_0^{\infty} \frac{1}{\left(x^2+A\right)^j} dx + \sum_{j=1}^{m} T_{j+n} \int_0^{\infty} \frac{1}{\left(x^2+B\right)^j} dx \right) \tag{19}$$

where the above integrals have the following solutions

$$\int_0^{\infty} \frac{1}{x^2+A} dx = \frac{\pi}{2\sqrt{A}} \tag{20}$$

calculated using the substitution

$$u = \frac{x}{\sqrt{A}} \tag{21}$$

and function $\arctan x$as the primitive function.

$$\int_0^{\infty} \frac{1}{\left(x^2+A\right)^2} dx = \frac{\pi}{4A^{3/2}} \tag{22}$$

The above integral can be calculated using the reduction formula:

$$\begin{aligned} \int \frac{dx}{\left(x^2+B\right)^2} &= \frac{x}{2B\left(x^2+B\right)} + \frac{1}{2B} \int \frac{dx}{x^2+B} \\ &= \frac{x}{2B\left(x^2+B\right)} + \frac{1}{2\sqrt{B^3}} \arctan \frac{x}{\sqrt{B}} \end{aligned} \tag{23}$$

taking the limits of integration from 0 to $\infty$.

## Case p = 1

In this case, the integral can be split into the two following integrals

$$\begin{aligned} J^{\hat{TP}}{}_{k,l} &= \frac{1}{a} \int_0^{2\pi} \frac{\left(a\cos\phi+b\right)-b}{\left(a\cos\phi+b\right)^n \left(1+\left(a\cos\phi+b\right)c^{TP}\right)^m} d\phi \\ &= \frac{1}{a} \int_0^{2\pi} \frac{d\phi}{\left(a\cos\phi+b\right)^{n-1} \left(1+\left(a\cos\phi+b\right)c^{TP}\right)^m} \\ &- \frac{b}{a} \int_0^{2\pi} \frac{d\phi}{\left(a\cos\phi+b\right)^n \left(1+\left(a\cos\phi+b\right)c^{TP}\right)^m} \end{aligned} \tag{24}$$

These integrals can then be calculated according to the case $p = 0$. Only the case $n-1 = 0$ requires additional calculations.

# 1. Integral $\hat{J}_{1,2}^{TP}$

Integral $\hat{J}_{1,2}^{TP}$ has the following form

$$\hat{J}_{1,2}^{TP} = \int_0^{2\pi} \frac{d\phi}{(a\cos\phi + b)^2 \left(1 + (a\cos\phi + b)\, c^{TP}\right)} \tag{25}$$

In this case $p = 0$, $n = 2$ and $m = 1$. Using the procedure derived in the introduction one can obtain

$$J_{1,2}^{\hat{T}P} = \frac{4}{a^2} \frac{1}{A_0^2 C_0} \int_0^{\infty} \frac{\left(x^2+1\right)^2}{\left(x^2+A\right)^2 \left(x^2+B\right)} dx \tag{26}$$

The partial fraction decomposition method for this integral is as follows

$$\begin{aligned}
\frac{\left(x^2+1\right)^2}{\left(x^2+A\right)^2 \left(x^2+B\right)} &= \frac{T_1}{x^2+A} + \frac{T_2}{\left(x^2+A\right)^2} + \frac{T_3}{x^2+B} \\
&= \frac{T_1 \left(AB + (A+B)x^2 + x^4\right)}{\left(x^2+A\right)^2 \left(x^2+B\right)} \\
&+ \frac{T_2 \left(B+x^2\right) + T_3 \left(A^2 + 2Ax^2 + x^4\right)}{\left(x^2+A\right)^2 \left(x^2+B\right)} \\
&= \frac{\left(T_1 AB + T_2 B + T_3 A^2\right)}{\left(x^2+A\right)^2 \left(x^2+B\right)} \\
&+ \frac{\left(T_1 (A+B) + T_2 + 2T_3 A\right)x^2}{\left(x^2+A\right)^2 \left(x^2+B\right)} \\
&+ \frac{(T_1 + T_3)\, x^4}{\left(x^2+A\right)^2 \left(x^2+B\right)}
\end{aligned} \tag{27}$$

The coefficients before $x^4, x^2, x^0$ must make the polynomials from numerators of both fractions equal. It allows to write a set of three equations as follows:

$$\begin{cases}
(1') & T_1 AB + T_2 B + T_3 A^2 = 1 \\
(2') & T_1 (A+B) + T_2 + 2T_3 A = 2 \\
(3') & T_1 + T_3 = 1
\end{cases} \tag{28}$$

where $T_1, T_2, T_3$ are the coefficients to be calculated. From the third equation

$$(3) \Rightarrow T_3 = 1 - T_1 \tag{29}$$

Applying Eq. (29) in the first equation

$$(1) \Rightarrow T_2 = \frac{1}{B}\left(1 - T_1 AB + (T_1 - 1)A^2\right) \tag{30}$$

$$T_2 = \frac{1}{B}\left(\left(1 - A^2\right) + T_1 \left(A^2 - AB\right)\right) \tag{31}$$

Then from the second equation, it is possible to derive $T_1$

$$(2) \Rightarrow BT_1(A+B)+(1-A^2)+T_1(A^2-AB)+2(1-T_1)AB=2B \tag{32}$$

$$T_1\left(BA+B^2+A^2-AB-2AB\right)=2B+A^2-1-2AB \tag{33}$$

$$T_1=\frac{A^2-1+2B(1-A)}{B^2-2AB+A^2}=\frac{A^2-1+2B(1-A)}{(B-A)^2} \tag{34}$$

So $T_3$ is equal

$$\begin{aligned} T_3 &= 1-T_1 \\ &= \frac{B^2-2AB+A^2}{(B-A)^2}-\frac{A^2-1+2B-2AB}{(B-A)^2} \\ &= \frac{B^2+1-2B}{(B-A)^2} \end{aligned} \tag{35}$$

$$T_3=\frac{B^2-2B+1}{(B-A)^2}=\frac{(B-1)^2}{(B-A)^2} \tag{36}$$

Then it is possible to derive $T_2$ coefficient

$$\begin{aligned} T_2 &= \frac{1}{B}\left(\left(1-A^2\right)+\frac{A^2-1+2B(1-A)}{(B-A)^2}\left(A^2-AB\right)\right) \\ &= \frac{1}{B}\frac{\left(1-A^2\right)(B-A)^2+\left(A^2-1+2B-2AB\right)A(A-B)}{(B-A)^2} \\ &= \frac{B-A-BA^2+A^3-A^3+A-2AB+2A^2B}{B(B-A)} \\ &= \frac{B-2AB+A^2B}{B(B-A)} \end{aligned} \tag{37}$$

$$T_2=\frac{1-2A+A^2}{B-A}=\frac{(1-A)^2}{B-A} \tag{38}$$

After having applied the partial fraction decomposition method, one can finally obtain

$$\begin{aligned} \tilde{J}_{1,2}^{TP} &= \frac{4}{a^2}\frac{1}{A_0^2C_0}\left(T_1\int_0^\infty\frac{dx}{x^2+A}+\right. \\ &+ \left. T_2\int_0^\infty\frac{dx}{(x^2+A)^2}+T_3\int_0^\infty\frac{dx}{x^2+B}\right) \\ &= \frac{4}{a^2}\frac{1}{A_0^2C_0}\left(T_1\frac{\pi}{2\sqrt{A}}+T_2I_2+T_3\frac{\pi}{2\sqrt{B}}\right) \end{aligned} \tag{39}$$

## 2. Integral $\hat{J}_{1,3}^{TP}$

$\hat{J}_{1,3}^{TP}$ is expressed as follows:

$$\hat{J}_{1,3}^{TP} = \int_0^{2\pi} \frac{d\phi}{(a\cos\phi+b)^2\left(1+(a\cos\phi+b)\,c^{TP}\right)^2} \tag{40}$$

In this case $p=0$, $n=2$, $m=2$. Applying the procedure from Introduction, one can obtain that

$$\hat{J}_{1,3}^{TP} = \frac{4}{a^2}\frac{1}{A_0^2C_0^2}\int_0^{\infty} \frac{\left(1+x^2\right)^3}{\left(x^2+A\right)^2\left(x^2+B\right)^2}dx \tag{41}$$

Using the partial fraction decomposition method:

$$\begin{aligned}
\frac{\left(1+x^2\right)^3}{\left(x^2+A\right)^2\left(x^2+B\right)^2} &= \frac{T_1}{x^2+A}+\frac{T_2}{\left(x^2+A\right)^2}+\frac{T_3}{x^2+B}+\frac{T_4}{\left(x^2+B\right)^2} \\
&= \frac{T_1\left(x^2+A\right)\left(x^2+B\right)^2+T_2\left(x^2+B\right)^2}{\left(x^4+A\right)^2\left(x^2+B\right)^2} \\
&+ \frac{T_3\left(x^2+A\right)^2\left(x^2+B\right)+T_4\left(x^2+A\right)^2}{\left(x^4+A\right)^2\left(x^2+B\right)^2} \\
&= \frac{\left(T_1AB^2+T_2B^2+T_3A^2B+T_4A^2\right)}{\left(x^2+A\right)^2\left(x^2+B\right)^2} \\
&+ \frac{x^2\left(T_1\left(B^2+2AB\right)+T_22B\right)}{\left(x^2+A\right)^2\left(x^2+B\right)^2} \\
&+ \frac{x^2\left(T_3\left(A^2+2AB\right)+T_42A\right)}{\left(x^2+A\right)^2\left(x^2+B\right)^2} \\
&+ \frac{x^4\left(\left(2B+A\right)T_1+T_2+T_3\left(2A+B\right)+T_4\right)}{\left(x^2+A\right)^2\left(x^2+B\right)^2} \\
&+ \frac{x^6\left(T_1+T_3\right)}{\left(x^2+A\right)^2\left(x^2+B\right)^2}
\end{aligned} \tag{42}$$

This leads to the four following equations with unknown coefficients $T_1, T_2, T_3, T_4$

$$\begin{cases}
(1'') & T_1AB^2+T_2B^2+T_3A^2B+T_4A^2=1 \\
(2'') & T_1\left(B^2+2AB\right)+2T_2B+T_3\left(A^2+2AB\right)+2T_4A=3 \\
(3'') & T_1\left(A+2B\right)+T_2+T_3\left(B+2A\right)+T_4=3 \\
(4'') & T_1+T_3=1
\end{cases} \tag{43}$$

Using the fourth equation one can obtain

$$(4) \Rightarrow T_3 = 1-T_1 \tag{44}$$

Then it is possible to rewrite equations $(1)$, $(2)$ and $(3)$ in a new form

$$\begin{cases} (1') & T_1\left(AB^2-A^2B\right)+T_2B^2+T_4A^2=1-A^2B \\ (2') & T_1\left(B^2+2AB-A^2-2AB\right)+2T_2B+2T_4A=3-A^2-2AB \\ (3') & T_1\left(A+2B-B-2A\right)+T_2+T_4=3-B-2A \end{cases} \tag{45}$$

From equation $(3')$ it is possible to derive the$T_4$coefficient

$$\left(3'\right) \Rightarrow T_4=3-B-2A-T_2-T_1(B-A) \tag{46}$$

Then after application formula for $T_4$ one can obtain

$$\begin{aligned} \left(2'\right) \quad \Rightarrow \quad & T_1\left(B^2-A^2\right)+2T_2B \\ + \quad & 2A\left(3-B-2A-T_2-T_1\left(B-A\right)\right)=3-A^2-2AB \end{aligned} \tag{47}$$

The above equation allows to derive $T_2$ coefficient

$$\begin{aligned} \Rightarrow \quad & T_1\left(B^2-A^2-2AB+2A^2\right)+T_2\left(2B-2A\right) \\ & =3-A^2-2AB-6A+2AB+4A^2 \end{aligned} \tag{48}$$

$$\Rightarrow T_1\left(B-A\right)^2+2T_2\left(B-A\right)=3\left(1-2A+A^2\right) \tag{49}$$

$$T_2=-\frac{1}{2}T_1\left(B-A\right)+\frac{3}{2}\frac{\left(A-1\right)^2}{B-A} \tag{50}$$

Now it is possible to rewrite equation $(1')$ by substituting $T_2$

$$\begin{aligned} \left(1'\right)T_1\left(AB^2-A^2B\right) \quad + \quad & B^2\left(-\frac{1}{2}T_1\left(B-A\right)+\frac{3}{2}\frac{\left(A-1\right)^2}{B-A}\right) \\ + \quad & A^2\left(3-B-2A-T_2-T_1\left(B-A\right)\right) \\ = \quad & 1-A^2B \end{aligned} \tag{51}$$

The above equation allows to derive the $T_1$ coefficient

$$\begin{aligned} T_1\left(AB^2-A^2B \quad - \quad \frac{1}{2}\left(B^2-A^2\right)\left(B-A\right)-A^2\left(B-A\right)\right) & \\ = \quad 1-A^2B-\frac{3}{2}\left(B^2-A^2\right)\frac{\left(A-1\right)^2}{B-A} & \\ - \quad 3A^2+A^2B+2A^3 & \end{aligned} \tag{52}$$

$$\begin{aligned} T_1\left(B-A\right)\left(AB-\frac{1}{2}\left(B^2-A^2\right)-A^2\right) \quad = \quad & 1-A^2B-\frac{3}{2}\left(B+A\right)\left(A-1\right)^2 \\ - \quad & 3A^2+A^2B+2A^3 \end{aligned} \tag{53}$$

$$\begin{aligned} T_1 (B-A)\left(2AB-B^2+A^2-2A^2\right) &= 2-3BA^2+6AB-3B-3A^3 \\ &+ 6A^2-3A-6A^2+4A^3 \end{aligned} \tag{54}$$

$$-T_1 (B-A)(B-A)^2 = 2-3A^2B+6AB-3B-3A+A^3 \tag{55}$$

$$T_1 = \frac{3A^2B+3B+3A-6AB-A^3-2}{(B-A)^3} \tag{56}$$

Now it is possible to obtain the full form of $T_2$ coefficient involving formula for $T_1$

$$\begin{aligned} T_2 &= -\frac{1}{2}T_1 (B-A)+\frac{3}{2}\frac{(A-1)^2}{B-A} = \\ &= \frac{2+A^3+6AB-3A-3B-3A^2B}{2(B-A)^2}+\frac{3}{2}\frac{\left(A^2-2A+1\right)(B-A)}{(B-A)^2} \\ &= \frac{2+A^3+6AB-3A-3B-3A^2B}{2(B-A)^2} \\ &+ \frac{3A^2B-6AB+3B-3A^3+6A^2-3A}{2(B-A)^2} \\ &= \frac{2-6A-2A^3+6A^2}{2(B-A)^2} \\ &= \frac{1-3A+3A^2-A^3}{(B-A)^2} \end{aligned} \tag{57}$$

$$T_2 = \frac{(1-A)^3}{(B-A)^2} \tag{58}$$

$T_1$ coefficient allows obtaining the full form of $T_3$ coefficient also

$$T_3 = 1-T_1 = \tag{59}$$

$$= \frac{B^3-3B^2A+3BA^2-A^3-3A^2B-3B-3A+6AB+A^3+2}{(B-A)^3} \tag{60}$$

$$T_3 = \frac{B^3-3AB^2-3B-3A+6AB+2}{(B-A)^3} \tag{61}$$

And at the end, it is possible to obtain full form of $T_4$ coefficient

$$
\begin{aligned}
T_4 &= 3-B-2A-T_2-T_1(B-A)= \\
&= 3-B-2A-\frac{(1-A)^3}{(B-A)^2}-\frac{3A^2B+3B+3A-6AB-A^3-2}{(B-A)^2} \\
&= \frac{(3-B-2A)\left(B^2-2AB+A^2\right)-\left(1-3A+3A^2-A^3\right)}{(B-A)^2} \\
&+ \frac{-3A^2B-3B-3A+6AB+A^3+2}{(B-A)^2} \\
&= \frac{3B^2-6AB+3A^2-B^3+2AB^2-A^2B-2AB^2}{(B-A)^2} \\
&+ \frac{4A^2B-2A^3-1+3A-3A^2}{(B-A)^2} \\
&+ \frac{A^3-3A^2B-3B-3A+6AB+A^3+2}{(B-A)^2} \\
&= \frac{3B^2-B^3-3B+1}{(B-A)^2} \\
&= \frac{B\left(3B-B^2-3\right)+1}{(B-A)^2}
\end{aligned} \tag{62}
$$

$$
T_4 = \frac{3B^2-B^3-3B+1}{(B-A)^2} \tag{63}
$$

Finally, the solution of the $\hat{J}_{1,3}^{TP}$ integral is as follows

$$
\hat{J}_{1,3}^{TP} = \frac{2\pi}{a^2}\frac{1}{A_0^2C_0^2}\left(\frac{T_1}{\sqrt{A}}+\frac{T_2}{2A^{3/2}}+\frac{T_3}{\sqrt{B}}+\frac{T_4}{2B^{3/2}}\right) \tag{64}
$$

# 3. Integral $\hat{J}_{2,2}^{TP}$

Integral $\hat{J}_{2,2}^{TP}$ has the following form

$$
\hat{J}_{2,2}^{TP} = \int_0^{2\pi}\frac{d\phi}{(a\cos\phi+b)\left(1+(a\cos\phi+b)c^{TP}\right)} \tag{65}
$$

In this case $p=0$, $n=1$ and $m=1$. Applying procedure from Introduction one can obtain

$$
\hat{J}_{2,2}^{TP} = \frac{4}{a}\frac{1}{A_0C_0}\int_0^{\infty}\frac{\left(1+x^2\right)dx}{\left(x^2+A\right)\left(x^2+B\right)} \tag{66}
$$

Partial fraction decomposition is like following

$$\begin{aligned}\frac{1+x^2}{(x^2+A)(x^2+B)} &= \frac{T_1}{x^2+A}+\frac{T_2}{x^2+B}\\ &= \frac{T_1\left(x^2+B\right)+T_2\left(x^2+A\right)}{(x^2+A)(x^2+B)}\\ &= \frac{(T_1B+T_2A)+(T_1+T_2)x^2}{(x^2+A)(x^2+B)}\end{aligned} \tag{67}$$

One can write the fraction in the following form

$$\frac{1+x^2}{(x^2+A)(x^2+B)} = \frac{(T_1B+T_2A)+(T_1+T_2)x^2}{(x^2+A)(x^2+B)} \tag{68}$$

After comparison of polynomials in numerators, one can write two equations with not known coefficients $T_1$ and $T_2$

$$\begin{cases} T_1B+T_2A=1 \\ T_1+T_2=1 \end{cases} \tag{69}$$

Solving this set of equations, it is possible to obtain coefficients $T_1$ and $T_2$

$$T_2 = 1-T_1 \tag{70}$$

$$T_1B+(1-T_1)A=1 \tag{71}$$

$$T_1 = \frac{1-A}{B-A} \tag{72}$$

$$T_2 = \frac{B-1}{B-A} \tag{73}$$

Then $\hat{J}_{2,2}^{TP}$ integral can be written in the following form

$$\hat{J}_{2,2}^{TP} = \frac{4}{a}\frac{1}{A_0C_0}\left(\frac{1-A}{B-A}\int_0^\infty \frac{dx}{x^2+A}+\frac{B-1}{B-A}\int_0^\infty \frac{dx}{x^2+B}\right) \tag{74}$$

Above integrals were calculated in the introduction. Finally, integral $\hat{J}_{2,2}^{TP}$ has the following solution

$$\hat{J}_{2,2}^{TP} = \frac{2}{a}\frac{1}{A_0C_0}\frac{1}{B-A}\left((1-A)\frac{\pi}{\sqrt{A}}+(B-1)\frac{\pi}{\sqrt{B}}\right) \tag{75}$$

# 4. Integral $\hat{J}_{2,3}^{TP}$

The integral $\hat{J}_{2,3}^{TP}$ is like following

$$\hat{J}_{2,3}^{TP} = \int_0^{2\pi}\frac{d\phi}{(a\cos\phi+b)\left(1+(a\cos\phi+b)c^{TP}\right)^2} \tag{76}$$

In this case $p=0$, $n=1$, $m=2$. After applying procedure from introduction one can obtain

$$\hat{J}_{2,3}^{TP} = \frac{4}{aA_0C_0^2}\int_0^{\infty}\frac{\left(1+x^2\right)^2 dx}{\left(x^2+A\right)\left(x^2+B\right)^2} \tag{77}$$

Then it is visible that integral $\hat{J}_{2,3}^{TP}$ has a similar form like integral $\hat{J}_{1,2}^{TP}$ by permuting A and B coefficients. Using the expression of $\hat{J}_{1,2}^{TP}$, one can obtain the solution of $\hat{J}_{2,3}^{TP}$.

$$\hat{J}_{2,3}^{TP} = \frac{2\pi}{a}\frac{1}{A_0C_0^2}\left(\frac{T_1}{\sqrt{B}}+\frac{T_2}{2B\sqrt{B}}+\frac{T_3}{\sqrt{A}}\right) \tag{78}$$

where coefficients $T_1, T_2, T_3$ are equal to, respectively

$$T_1 = \frac{B^2-1+2A\left(1-B\right)}{\left(A-B\right)^2} \tag{79}$$

$$T_2 = \frac{\left(1-B\right)^2}{A-B} \tag{80}$$

$$T_3 = \frac{\left(A-1\right)^2}{\left(A-B\right)^2} \tag{81}$$

# 5. Integral $\hat{J}_{3,2}^{TP}$

The integral $\hat{J}_{3,2}^{TP}$ is like following

$$\hat{J}_{3,2}^{TP} = \int_0^{2\pi}\frac{\cos\phi d\phi}{\left(a\cos\phi+b\right)^2\left(1+\left(a\cos\phi+b\right)c^{TP}\right)} \tag{82}$$

In this case $p=1$,$n=2$,$m=1$. After applying formula from Introduction

$$\begin{aligned}\hat{J}_{3,2}^{TP} &= \frac{1}{a}\int_0^{2\pi}\frac{d\phi}{\left(a\cos\phi+b\right)\left(1+\left(a\cos\phi+b\right)c^{TP}\right)} - \frac{b}{a}\int_0^{2\pi}\frac{d\phi}{\left(a\cos\phi+b\right)^2\left(1+\left(a\cos\phi+b\right)c^{TP}\right)} \\ &= \frac{1}{a}\hat{J}_{2,2}^{TP} - \delta\hat{J}_{1,2}^{TP}\end{aligned} \tag{83}$$

# 6. Integral $\hat{J}_{3,3}^{TP}$

The integral $\hat{J}_{3,2}^{TP}$ is like following

$$\hat{J}_{3,3}^{TP} = \int_0^{2\pi}\frac{\cos\phi d\phi}{\left(a\cos\phi+b\right)^2\left(1+\left(a\cos\phi+b\right)c^{TP}\right)^2} \tag{84}$$

In this case $p=1$,$n=2$, $m=2$. Applying formula from Introduction

$$\begin{aligned}\hat{J}_{3,3}^{TP} &= \frac{1}{a}\int_0^{2\pi}\frac{a\cos\phi+b}{\left(a\cos\phi+b\right)^2\left(1+\left(a\cos\phi+b\right)c^{TP}\right)^2}d\phi - \frac{b}{a}\int_0^{2\pi}\frac{d\phi}{\left(a\cos\phi+b\right)^2\left(1+\left(a\cos\phi+b\right)c^{TP}\right)^2} \\ &= \frac{1}{a}\int_0^{2\pi}\frac{d\phi}{\left(a\cos\phi+b\right)\left(1+\left(a\cos\phi+b\right)c^{TP}\right)^2} - \frac{b}{a}\hat{J}_{1,3}^{TP}\end{aligned} \tag{85}$$

Finally, one can write the solution of integral $\hat{J}_{3,3}^{TP}$ in the following way

$$\hat{J}_{3,3}^{TP} = \frac{1}{a}\hat{J}_{2,3}^{TP} - \delta\hat{J}_{1,3}^{TP} \tag{86}$$

# 7. Integral $\hat{J}_{4,2}^{TP}$

The integral $\hat{J}_{4,2}^{TP}$ is like following

$$\hat{J}_{4,2}^{TP} = \int_0^{2\pi} \frac{\cos\phi d\phi}{(a\cos\phi+b)\left(1+(a\cos\phi+b)c^{TP}\right)} \tag{87}$$

In this case $p=1$, $n=1$ and $m=1$. Applying formula from Introduction one can obtain

$$\begin{aligned}\hat{J}_{4,2}^{TP} &= \frac{1}{a}\int_0^{2\pi}\frac{d\phi}{\left(1+(a\cos\phi+b)c^{TP}\right)} - \frac{b}{a}\int_0^{2\pi}\frac{d\phi}{(a\cos\phi+b)\left(1+(a\cos\phi+b)c^{TP}\right)} \\ &= \frac{1}{a}\int_0^{2\pi}\frac{d\phi}{1+(a\cos\phi+b)c^{TP}} - \frac{b}{a}\hat{J}_{2,2}^{TP}\end{aligned} \tag{88}$$

After tangent half-angle substitution, the integral takes the form

$$\begin{aligned}\int_{-\infty}^{\infty}\frac{\frac{2}{1+x^2}dx}{ac^{TP}\left(\frac{1-x^2}{1+x^2}\right)+1+bc^{TP}} &= \int_{-\infty}^{\infty}\frac{2dx}{ac^{TP}(1-x^2)+(1+bc^{TP})(1+x^2)} \\ &= \int_{-\infty}^{\infty}\frac{2dx}{(1+bc-ac)x^2+(ac+1+bc)} \\ &= \frac{2}{ac+1+bc}\sqrt{\frac{ac+bc+1}{-ac+bc+1}}\pi \\ &= \frac{2\pi}{\sqrt{1+c(b+a)}\sqrt{1+c(b-a)}}\end{aligned} \tag{89}$$

Returning to $\hat{J}_{4,2}^{TP}$ integral

$$\hat{J}_{4,2}^{TP} = \frac{\frac{2\pi}{a}}{\sqrt{1+c(b+a)}\sqrt{1+c(b-a)}} - \frac{b}{a}\hat{J}_{2,2}^{TP} \tag{90}$$

Using constants $C_0$ and $D_0$, it is possible to write the final solution

$$\hat{J}_{4,2}^{TP} = \frac{2\pi}{a}\frac{1}{\sqrt{C_0D_0}} - \delta\hat{J}_{2,2}^{TP} \tag{91}$$

# 8. Integral $\hat{J}_{4,3}^{TP}$

Integral $\hat{J}_{4,3}^{TP}$ has the following form

$$\begin{aligned}\hat{J}_{4,3}^{TP} &= \int_0^{2\pi} \frac{\cos\phi\, d\phi}{(a\cos\phi+b)\left(1+(a\cos\phi+b)\,c^{TP}\right)^2} \\ &= \frac{1}{a}\int_0^{2\pi} \frac{d\phi}{\left(1+(a\cos\phi+b)\,c^{TP}\right)^2} \\ &- \frac{b}{a}\int_0^{2\pi} \frac{d\phi}{(a\cos\phi+b)\left(1+(a\cos\phi+b)\,c^{TP}\right)^2}\end{aligned} \tag{92}$$

Now it is possible to use tangent half-angle substitution

$$\hat{J}_{4,3}^{TP} = \frac{1}{a}\int_{-\infty}^{\infty} \frac{\frac{2}{1+x^2}dx}{\left(\left(1+bc^{TP}\right)+\left(ac^{TP}\right)\frac{1-x^2}{1+x^2}\right)^2} - \frac{b}{a}\hat{J}_{2,3}^{TP} \tag{93}$$

$$\begin{aligned}\int_{-\infty}^{\infty} \frac{\frac{2}{1+x^2}dx}{\left(\left(1+bc^{TP}\right)+\left(ac^{TP}\right)\frac{1-x^2}{1+x^2}\right)^2} &= \int_{-\infty}^{\infty} \frac{2dx\left(1+x^2\right)}{\left((1+bc)\left(1+x^2\right)+ac\left(1-x^2\right)\right)^2} \\ &= \int_{-\infty}^{\infty} \frac{2\left(1+x^2\right)dx}{\left(\left(1+c\left(b-a\right)\right)x^2+\left(1+c\left(b+a\right)\right)\right)} \\ &= 2\int_{-\infty}^{\infty} \frac{\left(1+x^2\right)}{\left(x^2+B\right)^2}dx\frac{1}{C_0^2}\end{aligned} \tag{94}$$

Now following integral must be calculated

$$\begin{aligned}\int_{-\infty}^{\infty} \frac{1+x^2}{\left(x^2+B\right)^2}dx &= \int_{-\infty}^{\infty} \frac{x^2+B+1-B}{\left(x^2+B\right)^2}dx \\ &= \int_{-\infty}^{\infty} \frac{dx}{x^2+B} + (1-B)\int_{-\infty}^{\infty} \frac{dx}{\left(x^2+B\right)^2} \\ &= \frac{\pi}{\sqrt{B}} + (1-B)\frac{\pi}{2B^{3/2}}\end{aligned} \tag{95}$$

Finally, the solution of the integral $\hat{J}_{4,3}^{TP}$ is as follows

$$\hat{J}_{4,3}^{TP} = \frac{\pi\left(B+1\right)}{aB^{3/2}}\frac{1}{C_0^2} - \delta\hat{J}_{2,3}^{TP} \tag{96}$$